Article

An Energetic and Topological Approach to Understanding the Interplay of Noncovalent Interactions in a Series of Crystalline Spiropyrrolizine Compounds

Dolma Tsering,[⊥] Pratik Dey,[⊥] Kamal K. Kapoor,* and Saikat Kumar Seth*

Read Online

ACCESS | Metrics & More | Article Recommendations | SI Supporting Information

ABSTRACT: Synthesis of quinoline-containing spiropyrrolizine was achieved via a 1,3-dipolar cycloaddition reaction of azomethine ylide (generated in situ from ninhydrin and L-proline) and (E)-2-styrylquinoline. The synthesized compounds were characterized by ^{1}H NMR, ^{13}C NMR, HRMS, and single-crystal XRD analysis. The XRD data revealed that the solid-state structures of the compounds belong to the monoclinic system of the space group $P2_1/c$ and are stabilized through various weak noncovalent interactions such as C−H···O, C−H···π, and π···π interactions. The noncovalent interactions are characterized and quantified through Hirshfeld surface analysis. Moreover, the interaction energies of the intermolecular noncovalent interactions are calculated through PIXEL calculation. The PIXEL calculation provides precise interaction energy with an energy decomposition scheme. Energy Framework calculations have also been performed to delve deeper into understanding the intermolecular interactions. The intermolecular interactions are further characterized using Bader's theory of "atoms in molecules" (QTAIM) and the "noncovalent" (NCI) interaction plot index. The nature and strength of noncovalent interactions are analyzed from the topological parameters at (3, −1) bond critical points (BCPs).
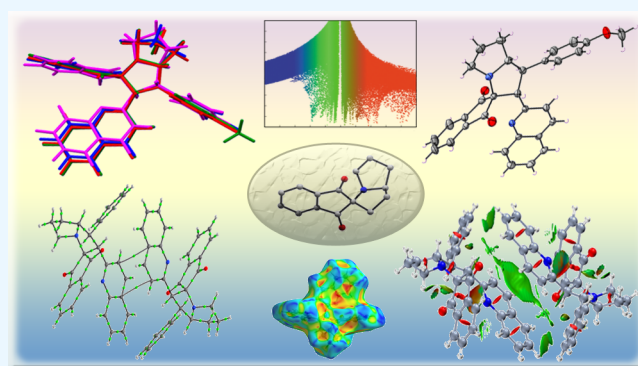
INTRODUCTION

Spiro compounds[1] have gained considerable attention due to their distinctive spiral framework, discovering broad utility across medicinal chemistry such as antibacterial,[2] antifungal,[3] cytotoxic,[4] anti-HIV,[5] antiproliferative,[6] antiviral,[7] and anti-cancer[8] properties. These compounds have been utilized in functional materials, including OLEDs with phosphine oxide components containing spiro structures,[9] light-emitting diodes,[10] fluorescent switches,[11] and optical data storage.[12] Among the various spiro compounds, spiropyrrolizines[13] emerge as captivating targets for synthesis due to their potential applications in both medicinal and material sciences. This dual significance has sparked keen interest among researchers in pursuing the synthesis of spiropyrrolizines. Of the various methods reported, the 1,3-dipolar cycloaddition reaction has proven itself as a reliable and efficient approach[14] with precise control over regio- and stereoselectivity. 1,3-Dipolar cyclo-addition reaction has extensively been used for generating five-membered nitrogen-containing heterocyclic compounds like pyrrolidines,[15] pyrrolizines,[16] dihydropyrroles,[17] and pyrroles.[18] We employed a 1,3-dipolar cycloaddition reaction to synthesize quinoline-containing spiropyrrolizines for growing crystals and gain insight into their noncovalent interactions.

Noncovalent interactions hold significant importance in the realms of chemical and biological processes.[19] They play an important role in shaping the structure of biomacromolecules like DNA and proteins and are involved in governing the complex molecular recognition process.[20] The organization of molecules deeply influences the properties of crystalline solids, and control over this organization defines the material's functional characteristics. Crystals spontaneously assemble, and the mutual interaction of molecules through various forces, particularly hydrogen bonding, often dominates crystal packing due to its high directionality. While hydrogen bonding is widely utilized in crystal packing, other weaker forces involving aromatic rings, such as C−H···π, π···π, anion···π, and lone-pair···π interactions, also play significant roles in crystal engineering.[21−23]

Spiropyrrolizine compounds are attracting increasing research interest due to their intricate structural complexity. While their

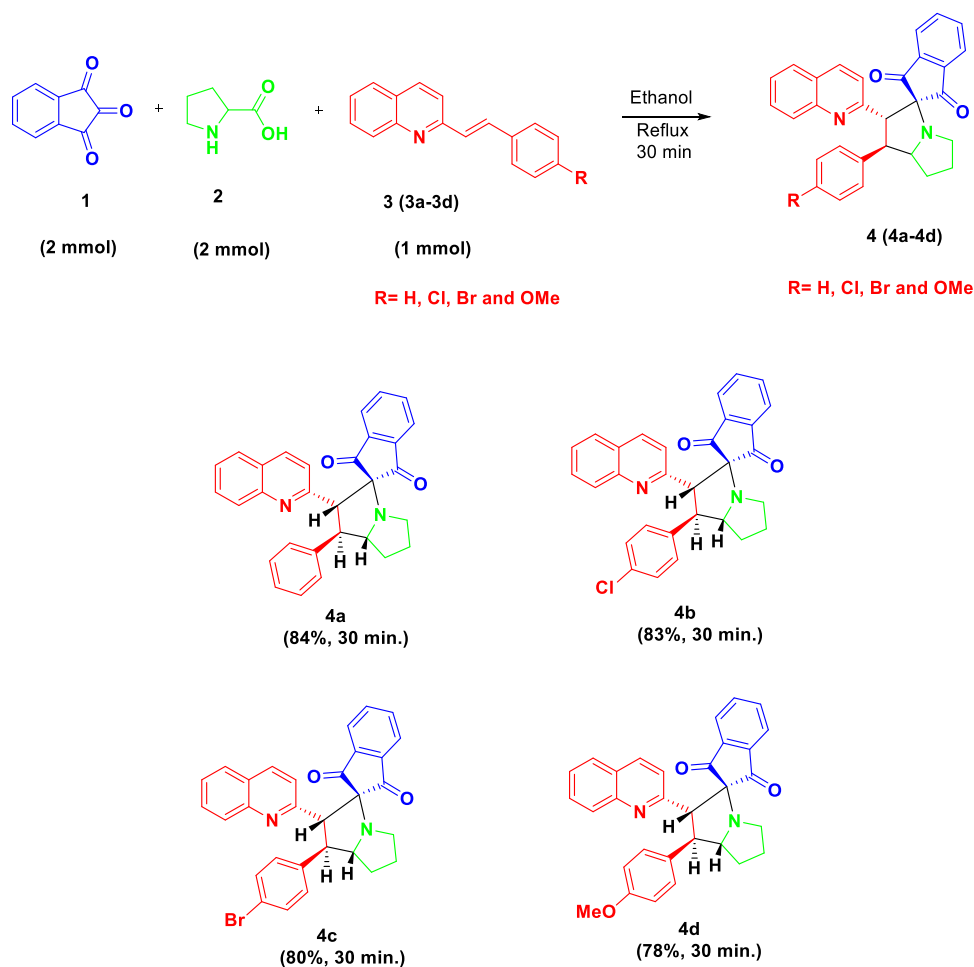**Scheme 1. Synthesis of Substituted Quinoline-Containing Spiropyrrolizines**

diverse bioactivities are well-established, a new focus is emerging. Researchers are delving deeper into understanding the relationship between their unique architecture and physiochemical behavior.[24,25] This deeper knowledge could unlock novel applications beyond their known biological effects, potentially impacting materials science, drug delivery, and molecular recognition.

In this study, we present the synthesis, structural characterization, and X-ray characterization of four quinoline-containing spiropyrrolizine compounds and examine their supramolecular assemblies and the involvement of weak forces in shaping their structures. The synthesized compounds have been characterized through ^{1}H NMR, ^{13}C NMR, DEPT135 NMR, HRMS, and SC-XRD (single-crystal X-ray diffraction). We have analyzed the noncovalent interactions by constructing the supramolecular framework. The noncovalent interactions are further characterized and quantified through Hirshfeld surface analysis.[26] The PIXEL method provides us with the interaction energies as well as lattice energies in a decomposed scheme.[27] Energy framework calculations provide further insight into intermolecular interactions. Bader's theory of "Atoms in molecules" (AIM)[28] and the "Non-covalent interaction" (NCI) plot index[29] are used to characterize non-covalent interaction. The analysis of topological parameters reveals the nature and strength of non-covalent interactions at the bond critical points.[30,31]

EXPERIMENTAL SECTION

Materials and Methods. All reagents used in the study were obtained from Sigma-Aldrich and were used without further purification. The progress of the reactions was tracked through thin-layer chromatography (TLC) employing silica-gel-coated aluminum sheets (60 F254, Merck). Visualization of spots was achieved by exposing the plates to ultraviolet (UV) light at 365 and 254 nm, and by treatment with iodine vapors. TLC plates were also treated with Dragon Dorff reagent. The ^{1}H NMR, ^{13}C NMR, and DEPT135 NMR spectra using CDCl$_3$ as the solvent were recorded on a Bruker AC-400 spectrometer operating at 400 MHz for ^{1}H and 100 MHz for ^{13}C/DEPT135 NMR, with tetramethylsilane (TMS) as the internal standard. Proton chemical shifts (δ) are reported in parts per million (ppm) relative to TMS. 'J' values are expressed in hertz (Hz). Notations such as s, d, t, q, and m in ^{1}H NMR spectra denote singlet, doublet, triplet, quartet, and multiplet, respectively. Uncorrected melting points (°C) were determined using an open glass capillary and a Perfit melting-point apparatus. High-resolution mass spectra (HRMS) were recorded using a Waters Xevo Q-TOF mass spectrometer. The formation of the racemic mixture was measured on an Agilent 1260 Infinity II HPLC instrument using Diacel Chiralpak IA, IB, and IF columns. Optical rotations were measured on a Rudolph Research Analytical, Autopol I.

Synthesis and Characterization. To begin with, a **1:1:1** mixture of ninhydrin (**1**), L-proline (**2**) and (*E*)-2-styrylquinoline (**3a**) was refluxed in ethanol for 30 min. The formation of

Scheme 2. Plausible Reaction Mechanism
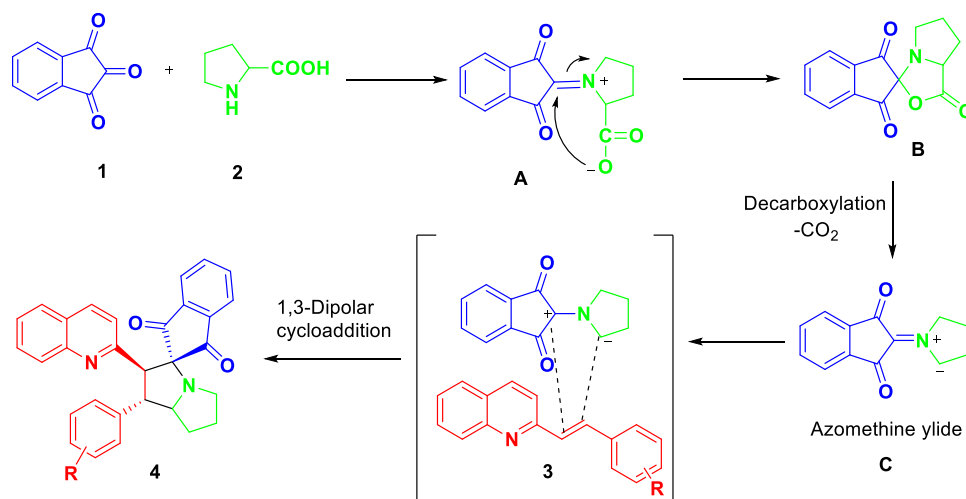
the desired product **4a** was observed in 42% yield. In an attempt to improve the yield of the product, another reaction with a **2:2:1** mixture of ninhydrin (**1**), L-proline (**2**), and (*E*)-2-styrylquinoline (**3a**) was performed under similar conditions. To our delight, a significant increase in the yield to 84% was observed. Similarly, other substrates (**4b–4d**) were synthesized using the same protocol as shown in Scheme 1. The structures of products **4a–4d** were established by ^{1}H NMR, ^{13}C NMR, DEPT135 NMR, HRMS, and SC-XRD analysis. In DEPT135 NMR, negative peaks at δ 48, δ 30, and δ 28 ppm correspond to the −CH$_2$ group of the pyrrolizine ring. The compounds are obtained as a racemic mixture as revealed by chiral HPLC (Figure S1) and a specific rotation measurement ([α] = 1), respectively.

Plausible Reaction Mechanism. The plausible mechanism is shown in Scheme 2. In this reaction, the nitrogen atom of proline **2** attacks the C2 carbonyl of ninhydrin **1** leading to iminium zwitterion **A** which undergoes intramolecular cyclization to form spiro compound **B**. Azomethine ylide **C**, formed by the decarboxylation of **B**, undergoes a 1,3 dipolar cycloaddition reaction with (*E*)-2-styrylquinoline **3**, leading to the formation of desired product **4**.

General Procedure for the Synthesis of Substituted (*E*)-2-Styrylquinolines (3a–3d). Synthesis of substituted (*E*)-2-styrylquinolines (**3a–3d**) has been carried out by following the earlier established protocol from our laboratory.[32] Structure elucidation of the synthesized compounds was confirmed by comparison with reported spectroscopic data.

General Procedure for the Synthesis of Substituted 1′-Aryl-2′-(quinolin-2-yl)-1′,2′,5′,6′,7′,7a′-hexahydrospiro-[indene-2,3′-pyrrolizine]-1,3-dione (4a–4d). A **2:2:1** mixture of ninhydrin **1** (2 mmol), L-proline **2** (2 mmol), and corresponding (*E*)-2-styrylquinoline **3** (1 mmol) was refluxed in ethanol (10 mL) for 30 min, and the progress of the reaction was monitored by TLC. After cooling, the solvent was evaporated under reduced pressure. The residue was transferred into a separatory funnel using ethyl acetate (30 mL) and washed with water (2 × 10 mL) and brine (1 × 10 mL). The organic layer was dried over anhydrous Na$_2$SO$_4$ and concentrated on a rotary evaporator. The crude product after column chromatography using an ethyl acetate and petroleum ether mixture gave the desired products **4a–4d** (78–84% yield).

Spectroscopic Characterization of Synthesized Compounds (4a–4d). *1′-Phenyl-2′-(quinolin-2-yl)-1′,2′,5′,6′,7′,7a′-hexahydrospiro[indene-2,3′-pyrrolizine]-1,3-dione (4a).* Yellow solid, Yield: 84% (0.372 g), mp 172–174 °C.

^{1}**H NMR** (400 MHz, CDCl$_3$) δ 8.06 (d, *J* = 7.2 Hz, 1H), 7.82–7.73 (m, 3H), 7.68 (d, *J* = 8.4 Hz, 1H), 7.54–7.48 (m, 3H), 7.38 (t, *J* = 7.5 Hz, 3H), 7.32–7.28 (m, 2H), 7.00 (d, *J* = 8.4 Hz, 1H), 6.68 (d, *J* = 8.4 Hz, 1H), 4.95 (d, *J* = 12.0 Hz, 1H), 4.20–4.08 (m, 2H), 2.88–2.83 (m, 1H), 2.79–2.73 (m, 1H), 2.17–2.10 (m, 1H), 2.00–1.88 (m, 3H). ^{13}**C NMR** (100 MHz, CDCl$_3$) δ: 203.65, 203.30, 156.21, 146.42, 142.78, 141.61, 140.20, 136.00, 135.35, 135.10, 129.03, 128.95, 128.73, 128.13, 127.68, 127.19, 127.14, 126.62, 125.95, 123.22, 121.95, 119.77, 75.23, 64.05, 53.82, 48.09, 30.81, 28.24. **HRMS** (ESI) *m/z*: [M + H]$^+$ calculated for C$_{30}$H$_{24}$N$_2$O$_2$, 445.1838; found 445.1941.

1′-(4-Chlorophenyl)-2′-(quinolin-2-yl)-1′,2′,5′,6′,7′,7a′-hexahydrospiro[indene-2,3′-pyrrolizine]-1,3-dione (4b). Yellow solid, Yield: 83% (0.396 g), mp 150–152 °C.

^{1}**H NMR** (400 MHz, CDCl$_3$) δ 8.05 (d, *J* = 7.2 Hz, 1H), 7.84–7.77 (m, 3H), 7.72 (d, *J* = 8.8 Hz, 1H), 7.55 (d, *J* = 8.0 Hz, 1H), 7.45–7.39 (m, 3H), 7.36–7.31 (m, 3H), 7.03 (d, *J* = 8.4 Hz, 1H), 6.64 (d, *J* = 8.4 Hz, 1H), 4.88 (d, *J* = 12.0 Hz, 1H), 4.18–4.09 (m, 2H), 2.93–2.89 (m, 1H), 2.79–2.75 (m,1H), 2.17–2.11 (m, 1H), 2.01–1.91 (m, 3H). ^{13}**C NMR** (100 MHz, CDCl$_3$) δ 202.61, 155.44, 146.45, 142.76, 141.45, 138.43, 136.22, 135.60, 135.31, 133.01, 129.47, 129.23, 129.18, 127.67, 127.27, 126.67, 126.16, 123.40, 122.11, 119.68, 77.24, 75.19, 64.09, 53.07, 48.15, 30.63, 28.26. **HRMS** (ESI) *m/z*: [M + H]$^+$ calculated for C$_{30}$H$_{23}$ClN$_2$O$_2$, 479.1448; found 479.1530.

1′-(4-Bromophenyl)-2′-(quinolin-2-yl)-1′,2′,5′,6′,7′,7a′-hexahydrospiro[indene-2,3′-pyrrolizine]-1,3-dione (4c). Yellow solid, Yield: 80% (0.417 g), mp 188–190 °C.

^{1}**H NMR** (400 MHz, CDCl$_3$) δ 8.04 (d, *J* = 7.2 Hz, 1H), 7.80–7.74 (m, 3H), 7.71 (d, *J* = 8.8 Hz, 1H), 7.54 (d, *J* = 8.0 Hz, 1H), 7.49 (d, *J* = 8.4 Hz, 2H), 7.41–7.35 (m, 3H), 7.32–7.28 (m, 1H), 7.04 (d, *J* = 8.4 Hz, 1H), 6.66 (d, *J* = 8.6 Hz, 1H), 4.88–4.83 (m, 1H), 4.11–4.07 (m, 2H), 2.87–2.82 (m, 1H), 2.77–2.71 (m, 1H), 2.14–2.09 (m, 1H), 1.98–1.87 (m, 3H). ^{13}**C NMR** (100 MHz, CDCl$_3$) δ: 203.38, 203.08, 155.66, 146.49, 142.65, 141.49, 139.26, 136.17, 135.50, 135.22, 132.08, 129.81, 129.19, 127.73, 127.24, 126.63, 126.11, 123.24, 122.01, 120.96, 119.69, 75.01, 64.00, 53.19, 48.04, 30.76, 28.28. **HRMS** (ESI)

Table 1. Crystal Data and Structure Refinement Parameters[a]

structure	compound 4a	compound 4b	compound 4c	compound 4d
CCDC number	2313165	2313166	2313167	2313168
empirical formula	$C_{30}H_{24}N_2O_2$	$C_{30}H_{23}ClN_2O_2$	$C_{30}H_{23}BrN_2O_2$	$C_{31}H_{26}N_2O_3$
formula Weight	444.51	478.95	523.41	474.54
temperature (K)	293(2)	293(2)	200(2)	200(2)
wavelength (Å)	1.54184	0.71073	0.71073	0.7103
crystal system	monoclinic	monoclinic	monoclinic	monoclinic
space group	$P2_1/c$	$P2_1/c$	$P2_1/c$	$P2_1/c$
a, b, c (Å)	11.149(2)	8.560(1)	8.522(1)	8.448(1)
	13.563(2)	22.557(2)	23.004(2)	23.373(2)
	15.532(2)	12.766 (2)	12.614(2)	12.628(1)
β (deg)	104.98(1)	103.07(1)	102.90(2)	102.80(1)
volume (Å^3)	2268.8(4)	2401.3(5)	2410.5(4)	2431.5(3)
Z/density (calc.) (Mg/m^3)	4/1.301	4/1.325	4/1.442	4/1.296
absorption coefficient (mm^{-1})	0.646	0.190	1.736	0.084
F(000)	936	1000	1072	1000
crystal size (mm^3)	0.36 × 0.34 × 0.22	0.15 × 0.15 × 0.08	0.15 × 0.14 × 0.14	0.15 × 0.15 × 0.14
limiting indices	$-13 \leq h \leq 12$,	$-10 \leq h \leq 10$,	$-9 \leq h \leq 10$,	$-10 \leq h \leq 10$,
	$-16 \leq k \leq 15$,	$-26 \leq k \leq 26$,	$-27 \leq k \leq 27$,	$-27 \leq k \leq 27$,
	$-16 \leq l \leq 18$	$-15 \leq l \leq 15$	$-14 \leq l \leq 14$	$-14 \leq l \leq 15$
reflections collected/unique	3245/3974	4127/3695	4233/3589	4215/3606
completeness to θ (%)	97.7	97.6	99.9	98.8
absorption correction	Gaussian	semiempirical from equivalents	semiempirical from equivalents	semiempirical from equivalents
max. and min transmission	0.87 and 0.80	0.99 and 0.97	0.78 and 0.77	0.99 and 0.99
refinement method	full-matrix least-squares on F^2	full-matrix least-squares on F^2	full-matrix least-squares on F^2	full-matrix least-squares on F^2
data/parameters	3974/307	4127/316	4233/316	4215/326
goodness-of-fit on F^2	1.043	1.031	1.049	1.112
final R indices $[I > 2\sigma(I)]$	$R_1 = 0.0628$,	$R_1 = 0.0847$,	$R_1 = 0.0482$,	$R_1 = 0.0954$,
	$wR_2 = 0.1558$	$wR_2 = 0.2239$	$wR_2 = 0.1013$	$wR_2 = 0.1970$
R indices (all data)	$R_1 = 0.0535$,	$R_1 = 0.0793$,	$R_1 = 0.0396$,	$R_1 = 0.0839$,
	$wR_2 = 0.1443$	$wR_2 = 0.2181$	$wR_2 = 0.0958$	$wR_2 = 0.1898$
largest diff. peak and hole (e Å^{-3})	0.717 and −0.318	0.626 and −0.359	0.704 and −0.678	0.578 and −0.229

[a]$R_1 = \sum ||F_o| - |F_c||/\sum |F_o|$, $wR_2 = [\sum\{(F_o^2 - F_c^2)^2\}/\sum\{w(F_o^2)^2\}]^{1/2}$, $w = 1/\{\sigma^2(F_o^2) + (aP)^2 + bP\}$, where $a = 0.0842$ and $b = 0.3822$ for compound **4a**, $a = 0.1221$ and $b = 1.8797$ for compound **4b**, $a = 0.0389$ and $b = 2.1240$ for compound **4c**, $a = 0.0663$ and $b = 3.1965$ for compound **4d**.
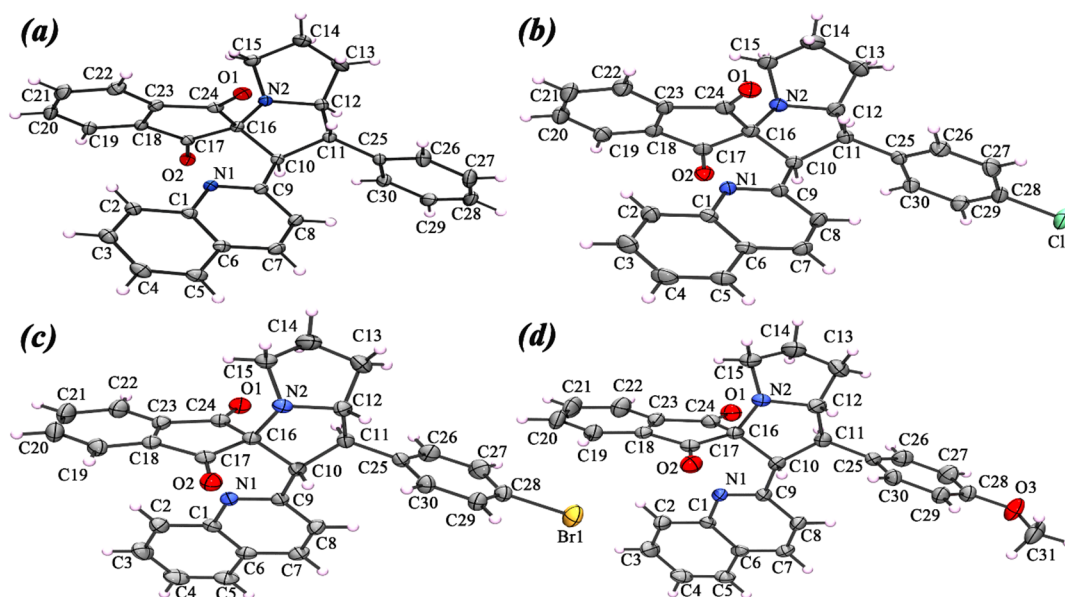

Figure 1. ORTEP diagram and atom numbering scheme of (a) compound **4a**, (b) compound **4b**, (c) compound **4c**, (d) compound **4d**. Thermal ellipsoids are drawn at the 30% probability level.

m/z: $[M + H]^+$ calculated for $C_{30}H_{23}BrN_2O_2$, 523.0943; found 523.1027.

1′-(4-Methoxyphenyl)-2′-(quinolin-2-yl)-1′,2′,5′,6′,7′,7a′-hexahydrospiro[indene-2,3′-pyrrolizine]-1,3-dione (4d). Yellow solid, Yield: 78% (0.369 g), mp 172−174 °C.

^{1}H NMR (400 MHz, CDCl₃) δ 8.05 (d, J = 7.2 Hz, 1H), 7.84−7.77 (m, 3H), 7.70 (d, J = 8.4 Hz, 1H), 7.54 (d, J = 8.0 Hz, 1H), 7.41 (d, J = 8.4 Hz, 2H), 7.37 (d, J = 7.2 Hz, 1H), 7.32 (d, J = 7.6 Hz, 1H), 6.99 (d, J = 8.0 Hz, 1H), 6.92 (d, J = 8.4 Hz, 2H), 6.68 (d, J = 8.4 Hz, 1H), 4.89 (d, J = 12.4 Hz, 1H), 4.20−4.19 (m, 1H), 4.08−4.03 (m, 1H), 3.83 (s, 3H), 2.90−2.88 (m, 1H), 2.79−2.73 (m,1H), 2.16−2.12 (m, 1H), 2.01−1.96 (m, 3H). ^{13}C NMR (100 MHz, CDCl₃) δ 203.53, 203.25, 158.69, 156.24, 146.40, 142.83, 141.54, 135.97, 135.39, 135.11, 131.98, 129.07, 129.02, 127.64, 127.20, 126.63, 125.95, 123.25, 121.96, 119.84, 114.35, 75.19, 64.20, 55.25, 53.08, 48.13, 30.74, 28.21. **HRMS** (ESI) m/z: $[M + H]^+$ calculated for $C_{31}H_{26}N_2O_3$, 475.1943; found 475.2081.

All of the NMR spectrum displays of compounds **4a−4b** are provided in Figures S2−S13.

X-ray Crystal Structure Determination. Single crystal X-ray diffraction intensity data were collected by using a SuperNova, Dual, Cu at home/near, Eos (for compound **4a**), and Bruker APEX-II CCD diffractometer (for compound **4b−4d**) equipped with graphite monochromated CuKα radiation (λ = 1.54184 Å) and MoKα radiation (λ = 0.71073 Å), respectively. Data reduction has been carried out using the CrysAlisPro 1.171.39.46e (for compound **4a**) and Bruker SAINT Program (for compound **4b−4d**), respectively.[33,34] An empirical absorption correction "Gaussian integration over a multifaceted crystal model"[33] (for compound **4a**), and SADABS[35] (for compound **4b−4d**) were applied. The structures of the compounds were solved by direct method and refined by the full-matrix least-squares technique on F^2 with anisotropic thermal parameters to describe the thermal motions of all non-hydrogen atoms using the programs SHELXT 2014/5 and SHELXL 2016/6, respectively.[36,37] All hydrogen atoms were located from the difference Fourier map and refined isotropically. All calculations were carried out using PLATON[38] and Olex2 program[39] respectively. Relevant crystal data and structure refinement parameters are listed in Table 1. CCDC 2313165 −213168 contains the supplementary crystallographic data for the title compounds (**4a−4d**).

Scheme 3. Schematic Diagram of Spiropyrrolizine Compounds
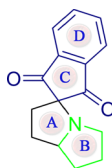
Hirshfeld Surface. Hirshfeld surface analysis[40−45] is valuable for exploring the packing modes and the intermolecular interactions in the molecular crystals. The Hirshfeld surface is unique for a set of spherical atom densities of a crystal. Hirshfeld surface color-coded maps of d_{norm} highlight the pinpoint of intermolecular natural shorter and longer interactions in the crystal structure. The d_{norm} is calculated by $= \frac{d_i - r_i^{vdw}}{r_i^{vdw}} + \frac{d_e - r_e^{vdw}}{r_e^{vdw}}$ based on d_i (distance to the nearest nucleus internal to the surface), d_e (the distance to the nearest nucleus external to the surface), and r_e^{vdw} (the van der Waals radius). The shape index (S) and the curvedness (C) on the basis of curvatures of the Hirshfeld surface at the point under analysis (κ_1 and κ_2) are defined by $S = \frac{2}{\pi}\arctan\left(\frac{\kappa_1 + \kappa_2}{\kappa_1 - \kappa_2}\right)$, and $C = \frac{2}{\pi}\ln\left(\frac{\kappa_1^2 + \kappa_2^2}{2}\right)^{1/2}$, respectively. The decomposed 2D fingerprint plots provide a percentage of intermolecular interactions, which allows quantified analysis of close contact within the crystal. To understand the various energetic components contributing to the total lattice energy (E_{tot}) of a crystal structure, computational studies were conducted using quantum chemistry methods. Specifically, the energy components—electrostatic energy (E_{ele}), polarization energy (E_{pol}), dispersion energy (E_{dis}), and repulsive energy (E_{rep})—were meticulously calculated through lattice energy framework analyses.[46] These analyses employed the CrystalExplorer 21 software suite to leverage its Tonto functionality. Within this computational framework, the energy framework diagram serves as a visual representation of the complex interplay between different types of energy within the crystal lattice. The diagram utilizes energy cylinders to depict these contributions, where the height and diameter of each cylinder correspond to the magnitude of the respective energy component. Notably, distinct color coding was employed for enhanced clarity: red cylinders are for electrostatic energy, green for dispersion energy, and blue for total energy, allowing for a straightforward interpretation of the relative contributions of these components to the overall stability of the lattice structure. The use of this energy framework approach facilitates a deeper understanding of intermolecular interactions and aids in predicting the stability and properties of the crystal structures.

Theoretical Calculation. The quantum chemical calculation to analyze the wave function has been carried out by using the Gaussian16 calculation package[47] with the DFT/B3LYP/6311++G(d,p) basis set. The intermolecular interaction energies for molecular dimers and Lattice energies of compounds **4a−4d** were decomposed into Coulombic, polarization, dispersion, and repulsion energy through the PIXELC method available in the CLP module.[48] In the PIXEL calculation, all hydrogen atoms are moved to their neutron distances. The interactions that play a crucial role in stabilizing the solid-state structures (interaction energies greater than −4 kJ/mol) have been considered for analysis using the PIXEL method. The B3LYP/6-311++G(d,p) basis set was used for accurate electron density calculations[49] by the Gaussian16 calculation package.[47] The topological analysis of the electron density has been carried out using Bader's theory of "Atoms in molecules"[50] by AIMALL software.[51] The relevant topological parameters such as electron charge density ($\rho(r)$) and the Laplacian of charge density $L(r) = \nabla^2\rho(r)$, local electron potential ($V(r)$), kinetic electronic energy density ($G(r)$), and total electronic energy density ($H(r) = V(r) + G(r)$) have been calculated using the theory of atoms in molecules proposed by Bader. The interaction energies of intermolecular interactions have been analyzed through the method shown by Espinosa,[52] i.e., interaction energy, $E_{int} = V(r)/2$. All the non-covalent interactions are further characterized by the "Noncovalent interaction" (NCI) plot[53] index using Multiwfn[54] and Visual Molecular Dynamics (VMD)[55] where the interactions are visualized through the colored isosurfaces. The strong, attractive interactions (ρ^- cut) and strong repulsion (ρ^+ cut) are represented by blue and red isosurfaces, whereas green

Table 2. Hydrogen Bonding Geometry (Å, °)

D−H···A	d(D−H)	d(H···A)	d(D···A)	∠D−H···A	symmetry
compound **4b**					
C7−H7···O2	0.93	2.57	3.412(4)	150	x, 1/2−y, −1/2+z
compound **4c**					
C7−H7···O2	0.95	2.54	3.396(3)	150	x, 3/2−y, −1/2+z
C11−H11···O1	1.00	2.59	3.226(3)	121	−
C14−H14B···O1	0.99	2.57	3.263(4)	127	−
C29−H29···O1	0.95	2.56	3.235(3)	128	x, 3/2−y, 1/2+z
compound **4d**					
C7−H7···O2	0.95	2.54	3.392(3)	150	x, 3/2−y, −1/2+z
C10−H10···O2	1.00	2.59	2.976(4)	103	−

Table 3. Geometrical Parameters for π−Stacking Interactions (Å, °)

rings i−j[a]	Rc[b]	R1v[c]	R2v[d]	α[e]	β[f]	γ[g]	symmetry	slippage
compound **4a**								
Cg(4)−Cg(4)	3.7547(12)	−3.5943(8)	−3.5944(8)	0	16.80	16.90	1−x, 1−y, 1−z	1.085
Cg(5)−Cg(7)	3.8021(16)	3.5099(9)	3.7288(13)	14.26(13)	11.26	22.61	1−x, 1/2+y, 3/2−z	−
Cg(7)−Cg(5)	3.8020(16)	3.7288(13)	3.5098(9)	14.26(13)	22.61	11.26	1−x, −1/2+y, 3/2−z	−

[a]Cg(4), Cg(5), and Cg(7) are the centroids of the [N1/C1/C5−C9] ring, [C1−C6] ring, and [C25−C30] ring, respectively, for compounds **4a**−**4d**. [b]Centroid distance between ring *i* and ring *j*. [c]Vertical distance from ring centroid *i* to ring *j*. [d]Vertical distance from ring centroid *j* to ring *i*. [e]Dihedral angle between the first ring mean plane and the second ring mean plane of the partner molecule. [f]Angle between centroids of the first ring and second ring mean planes. [g]Angle between the centroid of the first ring and the normal to the second ring mean plane of the partner molecule.

Table 4. Geometrical Parameters for C−H···π Interactions (Å, °)[a]

X−H···Cg	H···Cg	X···Cg	H···Perp	X−H···Cg	symmetry
compound **4b**					
C26−H26···Cg(4)	2.87	3.739(4)	−2.79	156	x, 1/2−y, 1/2 +z
compound **4c**					
C4−H4···Cg(7)	2.95	3.800(4)	−2.94	150	1+x, 3/2−y, −1/2+z
C30−H30···Cg(4)	2.85	3.726(3)	−2.79	153	x, 3/2−y, 1/2+z
compound **4d**					
C4−H4···Cg(7)	2.87	3.723(4)	−2.87	150	1+x, 3/2−y, −1/2+z
C30−H30···Cg(4)	2.92	3.796(4)	−2.85	154	x, 3/2−y, 1/2+z

[a]Cg(4) is the centroids of the [N1/C1/C6−C9] ring for compounds **4b**−**4d**. Cg(7) is the centroids of the [C25−C30] ring for compounds **4c**−**4d**.

isosurfaces represent weak attractive interactions.[53] The noncovalent interactions have further been characterized through colored spikes with the same color scheme in the RDG (Reduced Density Gradient) vs sign($\lambda_2\rho$) graph where the dimensionless RDG is defined by the term

$$\text{RDG}(r) = \frac{1}{2(3\pi^2)^{1/3}} \frac{|\Delta\rho(r)|}{\rho(r)^{4/3}}.^{53}$$

■ RESULTS AND DISCUSSION

Structural Description. The molecular views of compounds **4a**−**4d** are shown in Figure 1 with the atom numbering scheme. All the compounds are crystallized in a monoclinic space group P2$_1$/c with four molecules in each unit cell (Z = 4). Each compound contains a quinoline moiety, benzyl ring, nitrogen-containing pyrrolizine ring, and ninhydrin group. The difference between the compounds lies in the terminal aryl ring (C25−C30). The chlorine and bromine atoms are connected with the carbon C28 of the terminal aryl rings in compounds **4b** and **4c**, whereas in compound **4d**, the oxygen of the methoxy group binds to C28 (Figure S14). In crystallography, isostructurality is a key concept for evaluating structural similarities between distinct compounds. Unit cell dimensions

serve as crucial metrics in this analysis. Interestingly, compounds **4b**−**4d** exhibit remarkably similar unit cell dimensions, suggesting a potential isostructural relationship. To quantify this isostructurality, the isostructurality index (Π), developed by Fábián and Kálmán, was employed.[56,57] This index provides a numerical value reflecting the degree of structural similarity between the crystals. For compounds **4b**−**4d**, the calculated Π value is close to zero. Mathematically, the isostructurality index is expressed as Π = (a + b + c/a′ + b′ + c′) − 1, where a, b, and c represent the unit cell parameters of one crystal and a′, b′, and c′ represent those of the other. A Π value approaching zero signifies a high degree of structural similarity, implying isostructurality. The near-zero Π value for compounds **4b**−**4d** reinforces their structural congruence, confirming the initial observation based on unit cell dimensions. Bond lengths and bond angles for compounds **4a**−**4d** with esd are presented in Tables S1 and S2.

We have analyzed the geometric properties of compounds **4a**−**4d** and twenty-three spiropyrrolizine compounds retrieved from the CSD, identified by their respective CSD ref. codes: DIVBAN,[58] ECUDEO,[59] ELIHAI,[60] FATBEJ,[61] GOLGOG,[62] GOLGUM,[62] GOLHAT,[62] GONZER,[62] KIBOFOT,[63] KIBFUZ,[63] KIBRAR,[64] MAPFEP,[65] MOCSIK,[66] OMIWOW,[67]
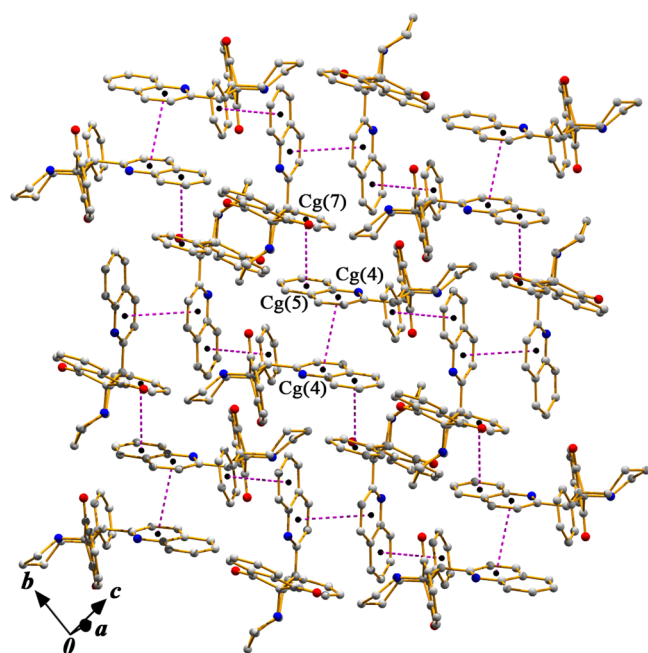
Figure 2. Supramolecular networks of compound **4a** were generated through the $\pi\cdots\pi$ stacking interactions.
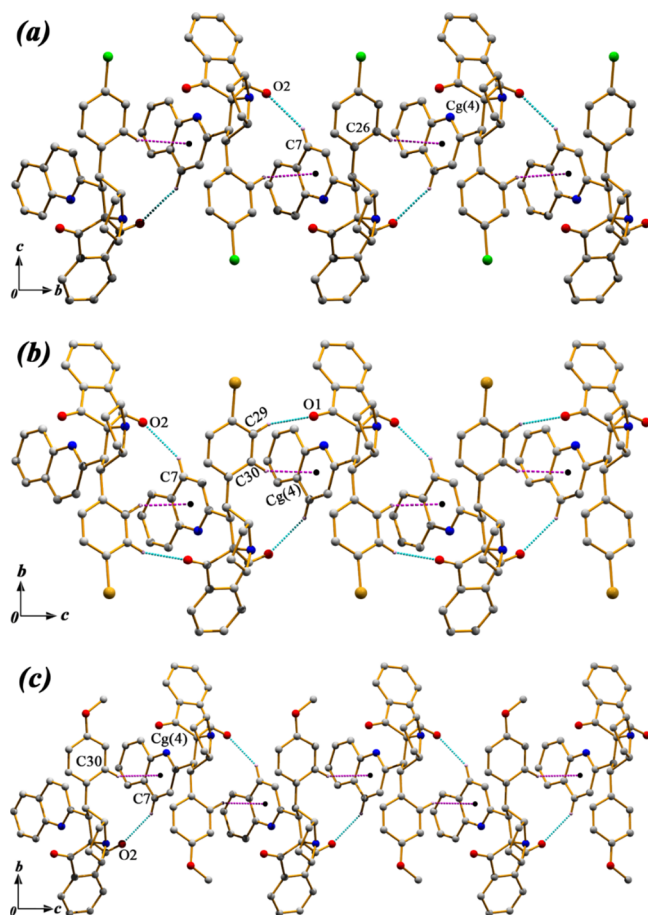
Figure 3. 1D supramolecular chains of (a) compound **4b**, (b) compound **4c**, and (c) compound **4d** generated through C−H⋯O and C−H⋯π interactions.

PIHNAX,[68] POFMED,[69] TEZQEV,[70] UDOMEI, UNOMAL,[71] WEVZUS,[72] XICFUL,[73] XICKAW,[74] and YEDVEM.[75] Our

analysis encompassed various parameters including bond distances, bond angles, and torsion angles (Tables S3 and S4). Notably, UDOMEI exhibited the highest C=O bond distance at 1.229 Å, while GOLGUM showed the maximum C=N bond distance at 1.479 Å. The range for C−C−O and C−C−N bond angles varied between 124.34° and 126.84° and 101.28° to 124.33°, respectively. Conversely, DIVBAN and POFMED displayed the shortest C=O bond length at 1.198 Å and C−N bond length at 1.437 Å, respectively. Similar trends were observed for compounds **4a**−**4d**, with their C=O and C−N bond distances falling within the range of 1.196 Å to 1.215 and 1.479 Å to 1.487 Å respectively, while their C−C−O and C−C−N bond angles ranged from 124.85° to 126.84° and 109.33° to 120.08° respectively. Additionally, we examined the angle between the two planes of rings A and B (Scheme 3). Furthermore, we calculated the highest deviation of carbon and the deviation of oxygen atoms from the mean plane of rings C and D (Scheme 3) across all compounds, as detailed in Table S5, where compounds **4a**−**4d** did not exhibit any exceptions. X−ray crystallographic study reveals that compound **4a** is stabilized through $\pi\cdots\pi$ interactions while C−H⋯O and C−H⋯π play the pivotal role in stabilizing compounds **4b**−**4d** (Tables 2, 3, and 4).

As shown in compound **4a**, the pyridine ring (N1/C1/C6−C9) of one moiety is juxtaposed to the pyridine ring of another moiety of the molecules at $(1-x, 1-y, 1-z)$ with a ring centroid separation distance of 3.7547(12) Å, corresponding to a ring offset of 1.085 Å. Again, this dimeric unit is further connected to the molecule at $(1-x, 1/2+y, 3/2-z)$ via $\pi\cdots\pi$ stacking interaction where the aryl ring (C1−C6) is juxtaposed to the terminal aryl ring (C25−C30) with a ring centroid separation distance of 3.8021(16) Å. Thus, the $\pi\cdots\pi$ stacking interactions lead to the formation of two-dimensional layered supramolecular structures (Figure 2).

X−ray crystallographic studies reveal that compounds **4b**−**4d** are stabilized through C−H⋯O and C−H⋯π interactions. In compound **4b**, the carbon atom C7 in the molecules at (x, y, z) acts as the donor to the oxygen atom O2 to the molecule at $(x, 1/2-y, -1/2+z)$. Besides C−H⋯O interactions, the molecule at (x, y, z) and $(x, 1/2-y, -1/2+z)$ is further connected with C−H⋯π interactions, where the carbon atom C26 of the terminal aryl ring in the molecule at (x, y, z) binds the centroid of the pyridine ring of the molecule at $(x, 1/2-y, 1/2+z)$. Thus, the molecules of compound **4b** interlink themselves through C−H⋯O and C−H⋯π interactions and generate a 1D chain along [010] direction (Figure 3a). In both compounds **4c** and **4d**, the carbon atom C30 is oriented toward the π−cloud of the pyridine ring in the at $(x, 3/2-y, 1/2+z)$. Furthermore, the carbon atom C7 of the molecule at (x, y, z) plays a pivotal role as a donor to the atom O2 of the molecule at $(x, 3/2-y, 1/2+z)$. Along with C7−H7⋯O2, the hydrogen bond C29−H29⋯O1 also helps stabilize compound **4c**. As a result, the C−H⋯O and C−H⋯π interactions in the compounds **4c** and **4d** help generate a 1D chain along [001] direction (see Figure 3b,c).

Again, the parallel chains of compounds **4c** and **4d** are further connected to C−H⋯π interactions where the carbon atom C4 binds the centroid of the terminal aryl ring of the molecule at $(1+x, 3/2-y, -1/2+z)$ lead to the formation of the 2D layered supramolecular structure (Figure 4).

Hirshfeld Surface and Fingerprint Plot Analysis. The Hirshfeld[76−80] surface analysis has been performed to explore the characteristics of the noncovalent interactions and quantify each noncovalent interaction's individual contribution to the
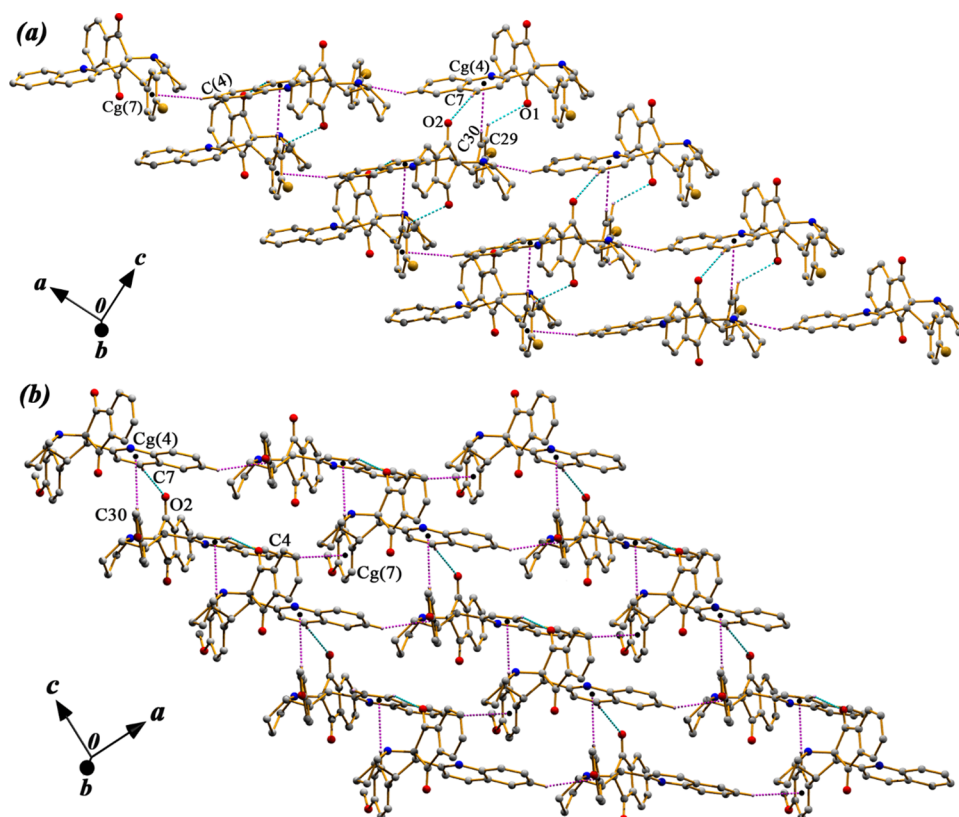
Figure 4. Layered supramolecular assemblies generated through C−H···O and C−H···π interactions of (a) compound **4c** and (b) compound **4d**.
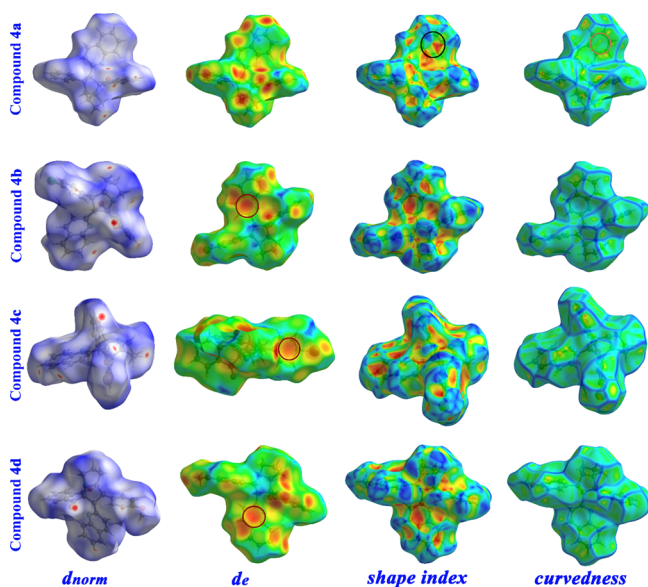
Figure 5. Hirshfeld surfaces mapped with d_{norm}, d_e, shape-index, curvedness of the compounds **4a**−**4d**.

Hirshfeld surface. In the Hirshfeld surface mapped over d_{norm}, the dark red spots around the donor and acceptor atoms indicate the presence of C−H···O hydrogen bond interactions in compounds **4b**−**4d** (Figure 5). Some other spots on the d_{norm} surfaces correspond to H···H close contacts and nonclassical hydrogen bond interactions. The convex and concave regions in the shape index are illustrated by blue and red triangles, respectively. The molecular intricacies of compound **4a** are elegantly unveiled through a detailed examination of π···π

interactions, as illustrated in Figure 5. The shape index surface presents an array of touching complementary pairs of triangles upon undergoing a 180° rotation. This particular geometric configuration is a hallmark of π···π stacking, a fundamental noncovalent interaction that is integral to the molecular stability and self-assembly of aromatic compounds. The significance of π···π[81] stacking cannot be overstated, as it is a critical factor in the molecular architecture of compound **4a**. These interactions are characterized by the alignment of electron-rich regions of adjacent aromatic rings, facilitating a stabilizing force that contributes to the compound's structural integrity and its propensity for self-organization. Further evidence of π···π interactions is discernible on the curvedness surfaces associated with compound **4a**. The flat surface area represents zones where the electron clouds of neighboring aromatic rings are in close proximity, enabling the occurrence of π···π interactions. The visualization of these interactions on the molecule is not merely a structural detail but a testament to their pivotal role in influencing the overall molecular conformation and potential reactivity of compound **4a**. The contribution to the total Hirshfeld surface area due to π···π stacking interaction is 7.9% ($d_i = d_e = 1.928$ Å) in compound **4a,** while the π···π stacking interaction comprises only 0.2% each for compounds **4b**−**4d**. Again, the bright-orange colors above the π−electron clouds (brown encircled) of the d_e surface map characterize the C−H···π interactions in compounds **4b**−**4d** (Figure 5).

The decomposed scattered points of 2D fingerprint plots are shown in Figure 6, which are used to quantify the individual contributions of each interaction. The wings in the donor ($d_e > d_i$) and acceptor ($d_i > d_e$) regions of compounds **4b**−**4d** represent the C···H/H···C interaction corresponding to the C−H···π interaction. These wings in the region of ($d_i = 2.088$ Å; $d_e =$
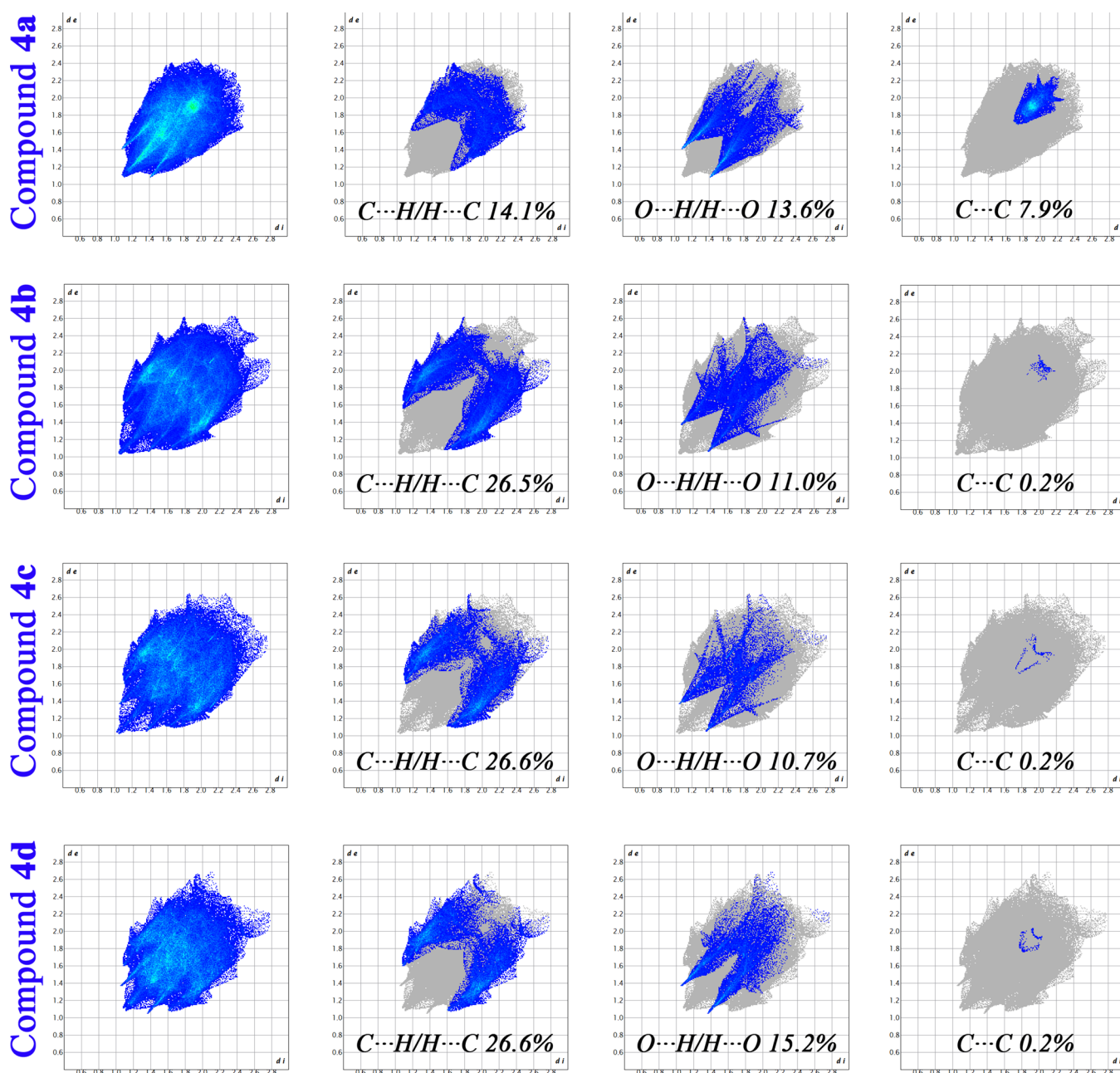
Figure 6. Fingerprint plot of Full, C⋯H/H⋯C, O⋯H/H⋯O, and C⋯C interactions of the compounds **4a−4d**.

Table 5. Calculated Lattice Energy (kJ/mol) for Compounds 4a−4d

compounds	E_{Coul}	E_{Pol}	E_{Disp}	E_{Rep}	E_{Total}
compound **4a**	−75.4	−31.8	−201.1	183.5	−124.9
compound **4b**	−78.7	−34.8	−207.3	176.0	−144.8
compound **4c**	−86.1	−34.4	−211.2	193.9	−137.8
compound **4d**	−86.2	−36.0	−211.8	184.9	−149.1

1.217 Å) and (d_i = 2.088 Å; d_e = 1.237 Å) contribute 26.6% each for compound **4c−4d** and 26.5% contribution (d_i = 2.108 Å; d_e = 1.237 Å) for compound **4b** of the total Hirshfeld surface area. Only 14.1% contribution of C⋯H/H⋯C interaction of the total Hirshfeld surface area is evidenced in the region of (d_i = 2.414 Å; d_e = 1.642 Å) of compound **4a**. Another weak C−H⋯O intermolecular interaction appears as very small spikes of almost equal lengths in the two-dimensional fingerprint plots (Figure

6). The O⋯H/H⋯O interactions comprise 13.6% (d_i = 1.402 Å; d_e = 1.086 Å), 11.0% (d_i = 1.377 Å; d_e = 1.066 Å), 10.7% (d_i = 1.367 Å; d_e = 1.051 Å) and 15.2% (d_i = 1.367 Å; d_e = 1.053 Å) of the total Hirshfeld surface of the compounds **4a−4d**, respectively. Significant contributions are found from Cl⋯H/H⋯Cl (9.2%) and Br⋯H/H⋯Br (9.6%) in compounds **4b** and **4c**, respectively (Figure S15). The N⋯H/H⋯N interactions comprise 2.6 and 3.0% in compounds **4a** and **4b** to the Hirshfeld surface, whereas in both compounds **4c** and **4d**, the N⋯H/H⋯N interactions contribute 3.1% each of the total Hirshfeld surface (Figure S15). A significant difference between the molecular interactions in the compounds in terms of H⋯H interactions is reflected in the distribution of scattered points in the fingerprint plots, which spread only up to d_i = d_e = 1.086 Å in compound **4a**, d_i = d_e = 1.036 Å in compound **4b**, d_i = d_e = 1.041 Å in compound **4c** and d_i = d_e = 1.121 Å in compound **4d**. Some

other negligible contributions come from O⋯C/C⋯O, N⋯C/C⋯N, etc., which are also represented in Figure S15.

An exhaustive analysis of the Hirshfeld surfaces has been conducted for a series of spiropyrrolizine compounds with CSD ref. codes: DIVBAN,[57] ECUDEO,[58] ELIHAI,[59] FATBEJ,[60] GOLGOG,[61] GOLGUM,[61] GOLHAT,[61] GONZER,[61] KIBO-FOT,[62] KIBFUZ,[62] KIBRAR,[63] MAPFEP,[64] MOCSIK,[65] OMIWOW,[66] PIHNAX,[67] POFMED,[68] TEZQEV,[69] UDO-MEI, UNOMAL,[70] WEVZUS,[71] XICFUL,[72] XICKAW,[73] and YEDVEM,[74] sourced from the Cambridge Structural Database (CSD). The investigation primarily focuses on the d_{norm} surface, which serves as a critical indicator of hydrogen bonding interactions within these compounds. As illustrated in Figure S16, the prevalence of hydrogen bonding reaffirms its pivotal role in the structural behavior of spiropyrrolizines. Additionally, detailed elucidation of the quantification of intermolecular interactions is provided through a bar chart depiction in Figure S17. Notably, the contributions of various interactions such as C⋯H/H⋯C, O⋯H/H⋯O, C⋯C, and N⋯H/H⋯N range from 7.2 to 24.5, 9.5−37.7, 0.0−7.9, and 1−5.8%, respectively, for compounds retrieved from CSD (Figure S18). Simultaneously, for compounds **4a−4d**, these contributions vary within a range of 14.1−26.6, 10.7−15.2, 0.2−7.9, and 2.6−3.1%, respectively, indicating distinctive intermolecular interaction profiles across the analyzed compounds.

Energy Decomposition Analysis of Dimeric Molecular Pairs in the Crystal Structures. *Molecular Pairs of Compound 4a*. To investigate the significant interactions to stabilize the crystal structures, we obtained eight molecular pairs in compound **4a**. The interaction energies of the MPs (Figure 7) vary from −44.9 to −8.5 kJ/mol (Table S6). The most stable dimeric unit is MP 1, which is stabilized through the C−H⋯O, C−H⋯C, and H⋯H interactions[57,82] with an interaction energy of −44.9 kJ/mol. The molecular pairs MP 2 and MP 3 have interaction energies of −23.8 and −23.0 kJ/mol, respectively. The molecular pair MP 2 is stabilized through C⋯C and H⋯H interactions, respectively, where C−H⋯O, C−H⋯N, and H⋯H have played a pivotal role in stabilizing the dimer MP 3. The interactions of the dimeric units MP 1, MP 2, and MP 3 are predominantly dispersive in nature with 58.4, 65.4, and 59.4% contributions toward stabilization. The molecular pair of MP 4 is also stabilized (E_{Total} = −19.4 kJ/mol) through C−H⋯O, H⋯H, C⋯C interactions. The interaction energies of MP 5 and MP 6 are also dispersive in nature, with 60.2 and 73.8% contributions toward stabilization. The C−H⋯O interactions (E_{Total} = −15.7 kJ/mol) play a crucial role in the molecular pair MP 5 whereas H⋯H, C⋯C interactions (E_{Total} = −12.2 kJ/mol) stabilized the dimeric unit MP 6. The molecule at symmetry (x, y, z) binds with the molecule in the symmetry ($-x+1$, $-y+1$, $-z+2$) (see MP 7), and (x, $-y+1/2$, $z+1/2$) (see MP 8) are also dispersive in nature (87.8, 58.7%) with H⋯H (E_{Total} = −10.1 kJ/mol) and C−H⋯O, H⋯H interactions (E_{Total} = −8.5 kJ/mol), respectively.

Molecular Pairs of Compound 4b. The investigation of interaction energies for the molecular pairs (MPs) revealed eight molecular pairs of compound **4b** (Figure 8). The interaction energies of all the molecular pairs have been summarized in Table S6. The C−H⋯O and C−H⋯C interactions (E_{Total} = −47.9 kJ/mol) stabilize the molecular dimer MP 1 whereas the molecular pair MP 2 stabilizes through C−H⋯O, C−H⋯C, as well as H⋯H interactions (E_{Total} = −24.0 kJ/mol). In MP 3, H⋯H and O⋯C (E_{Total} = −18.2 kJ/mol) play a pivotal role in stabilization, while the molecular pairs MP 4, MP 5, and MP 6

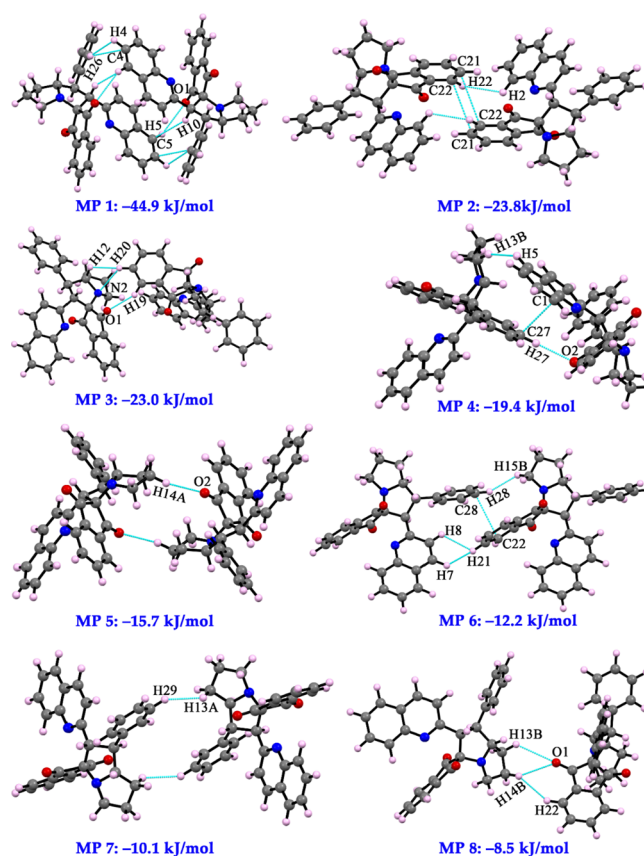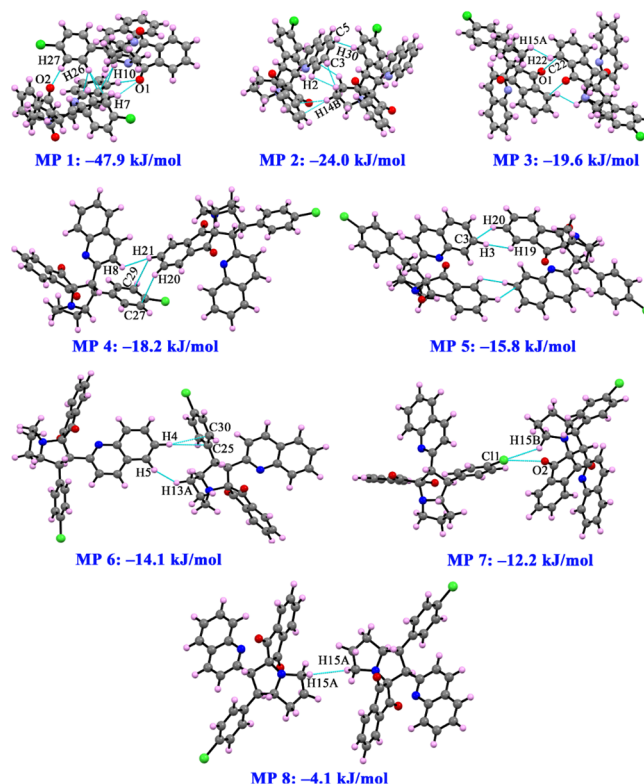**Figure 7.** Molecular dimers observed in compound **4a**.

Figure 8. Molecular dimers observed in compound **4b**.

are stabilized through H⋯H and C−H⋯O interactions. The molecular pair MP 1 is less dispersive in nature than the other
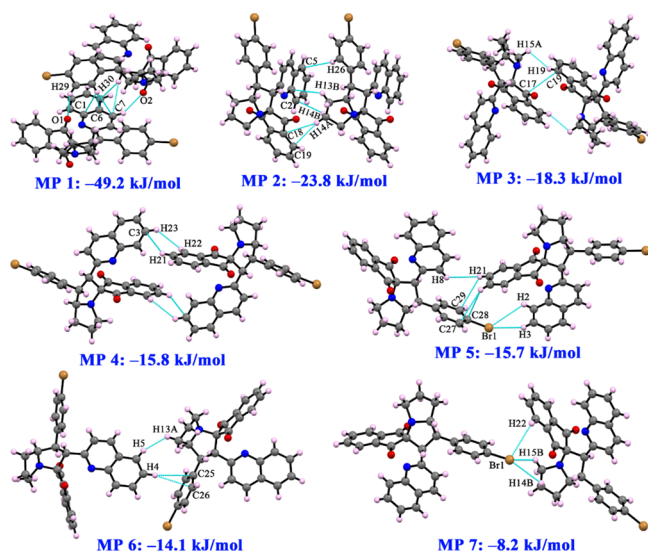
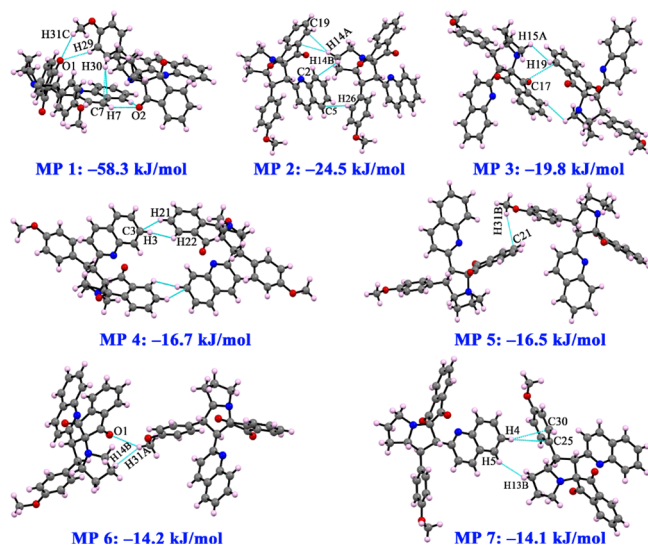**Figure 9.** Molecular dimers observed in compound **4c**.

Figure 10. Molecular dimers observed in compound **4d**.

molecular pairs. The interactions of dimeric units MP 2 and MP 3 are dispersive in nature with 65.2 and 60.3% contribution toward stabilization. The dispersion energies vary from 76.3 to 65.2% for stabilizing the dimeric units MP 4, MP 5, and MP 6. The dispersive interactions C−H···Cl, Cl···O (for MP 7:64.8%), and H···H (for MP 8:86.8%) contribute −12.2 and −4.1 kJ/mol, respectively.

Molecular Pairs of Compound 4c. Seven molecular pairs are extracted to investigate the interaction energies of compound **4c** (Figure 9). The interaction energies lie between −52.0 and −14.1 kJ/mol (see Table S6). The molecule at (x, −y+3/2, z − 1/2) has the shortest Cg···Cg distance of 7.418 Å bind with the molecule at (x, y, z) through C−H···O and C−H···C interactions (E_{Total} = −49.2 kJ/mol; dispersivity: 57.7%). The C−H···C interactions (E_{Total} = −23.8 kJ/mol) stabilize the dimer MP 2, which is also dispersive in nature (66.6%). The interactions H···H and C···C help the dimeric unit MP 3 (E_{Total} = −18.3 kJ/mol) to stabilize (dispersivity: 59.8%). The H···H and C−H···C interactions play a pivotal role in stabilizing molecular pairs MP 4 and MP 6 with total interaction energies of −15.8 and −14.1 kJ/mol. The dispersive interactions H···H, C−

H···C, C−H···Br contribute −15.7 kJ/mol of total interaction energy toward the stabilization of MP 6 while only −8.2 kJ/mol interaction energy is contributed by C−H···Br interactions in MP 7. All the interactions that stabilize the molecular pair MP 4−MP 5 are dispersive in nature, with contributions varying between 55.7 and 75.3%.

Molecular Pairs of Compound 4d. Investigation of the interaction energy of intermolecular interactions of Compound **4d** has been performed by choosing seven molecular pairs (Figure 10) whose interaction energies vary from −52.0 to −4.7 kcal/mol (Table S6). The most stable molecular pair MP 1 is stabilized through C−H···O, and C−H···C interactions with interaction energy −52.0 kJ/mol. The interactions of dimeric units MP 1 are predominantly dispersive in nature, with a 55.1% contribution toward stabilization. The C−H···C interactions along with H···H interactions stabilize the molecular pairs MP 2, MP 4, MP 6, and MP 7 with interaction energies −24.5, −16.7, −14.2, and −14.1 kJ/mol, respectively. The dispersivity of C−H···C and H···H interactions vary from 57.3 to 69.7%. Dispersive interactions (61.4%) C···C, and H···H stabilize the molecular pair MP 3 (E_{Total} = −19.8 kJ/mol), whereas only C−H···C interaction helps to stabilize the dimeric unit MP 5 (E_{Total} = −16.5 kJ/mol; dispersivity: 72.9%).

Lattice Energies and Energy Framework. In the realm of crystallography and solid-state chemistry, lattice energies[83,84] serve as a pivotal metric for quantifying the strength and extent of interactions within a crystalline network. These energies are not merely indicative of the cohesive forces at play but also provide a comparative framework to assess the stability of different compounds. The computation of the total lattice energy for a given molecule is a complex endeavor that necessitates a nuanced understanding of theoretical models that approximate intermolecular potential energies. In this context, the title molecules' lattice energy was meticulously calculated by employing a robust theoretical framework designed to evaluate these potential energies with precision.

The study of lattice energies provides profound insight into the intermolecular forces that govern the stability of crystalline compounds. In the case of compounds **4a−4d**, a meticulous examination of their lattice energies reveals a notable variance, as detailed in Table 5. The energies range from −124.9 to −149.1 kJ/mol, indicative of the nuanced differences in intermolecular interactions across these compounds.

Table 5 presents the lattice energies in a decomposed format, categorizing them into Coulombic, polarization, dispersion, and repulsion components. Such a breakdown is essential for a granular understanding of the forces at play. Notably, all four compounds exhibit a pronounced dominance of dispersion energy over electrostatic energy, which aligns with the general expectations for organic molecules, where dispersion forces are typically the most significant contributors to lattice stability.

The dispersion energy's contribution to the overall lattice stabilization is quantitatively significant. For compound **4a**, it accounts for 65.2% of the total lattice energy, while for compound **4b**, it constitutes 64.6%. This trend is consistent, albeit with slight variations, for compounds **4c** and **4d**, where the dispersion energies contribute 63.6 and 63.4%, respectively. These percentages not only highlight the supremacy of dispersion forces in these structures but also suggest a relative uniformity like these organic compounds' intermolecular interactions.

In the context of the energy framework, the electrostatic, polarization, dispersion, repulsion, and total energies were

determined by analyzing the structural cluster within a radius of 3.8 Å. The cylindrical tube's radius (Figure 11) within the energy structure serves as an indicator of the relative magnitude of each energy component. The tube's dimensions are calibrated using a scale factor of 100. The scale factors for the energy framework calculations are set to K_{ele}= 1.057, K_{pol}= 0.740, K_{dis}= 0.871, K_{rep}= 0.618, with a cutoff value of 5 kJ/mol within 3 × 3 × 3 unit cells.[46] As depicted in Figure 11, it is evident that for compounds **4a−4d**, the dispersion energies have a more substantial impact on the total energy than the Coulombic energies. These observations (Figure S19) corroborate the lattice energy estimations obtained via the PIXELC method.

The implications of such findings are manifold. They underscore the importance of considering dispersion forces in the computational modeling and design of new materials. Furthermore, the significant Coulombic contributions observed suggest that electrostatic interactions, while secondary to dispersion forces, are nonetheless integral to the compounds' stability. This nuanced understanding of lattice energies can inform the synthesis of compounds with desired properties and guide future research in materials science and crystal engineering.

NCI Analysis. We have further analyzed and characterized the noncovalent interactions involved in the supramolecular structures by the "noncovalent interaction" (NCI) plot index. We have chosen the same models that have been used in the QTAIM calculation. The interactions are represented by the colored isosurfaces, which have been differentiated by a red-yellow-green-blue color scale. In Figure 12a,b, the stretched green isosurfaces (marked by the black arrows) represent the $\pi\cdots\pi$ interactions in compound **4a**. The green spikes in the RDG vs sign($\lambda_2\rho$) graph (Figure S20a,b) also confirm the presence of weak interaction. The presence of C−H⋯π interactions in the compounds **4b−4d** is also confirmed by the green patches (marked by blue arrows) (Figure 12c−g). From PIXEL calculation, we have seen that $\pi\cdots\pi$ and C−H⋯π interactions are strongly dispersive in nature, which is also confirmed by the presence of the stretched green iso-surfaces; the more it is stretched, the more dispersive it is in nature. In Figure 12c−g, the bluish-green isosurfaces (marked by red arrows), as well as bluish-green spikes in the scattered graph (Figure S20c−g), represent the C−H⋯O interactions. The bluishness in the iso-surfaces as well as in the spikes of RDG vs sign($\lambda_2\rho$) graph strongly suggest that the C−H⋯O interactions are stronger than the $\pi\cdots\pi$ and C−H⋯π interactions. All the prominent colored iso-surfaces and their respective spikes in the RDG vs sign($\lambda_2\rho$) graph analyzed by the NCI plot index verified the existence of these noncovalent interactions observed in structural studies.

QTAIM Calculation. The noncovalent interactions have been analyzed through Bader's theory of "Atoms in molecules" (QTAIM). Figure 13 shows the AIM models, which are part of the self−assembled structures (Figures 2−4) of the compounds. The black dotted lines connecting two atoms are the bond path that characterizes the presence of noncovalent interactions. The green spheres represent the bond critical points (BCPs) where the charge density gradient is the minimum. The symmetry properties along the interaction direction are revealed by examining ellipticity (ε) values, which are determined by the ratio of the absolute magnitudes of the first (λ_1) and second (λ_2) eigenvalues of the Hessian matrix of the electron density at a bond critical point: $\varepsilon = |\lambda_1|/|\lambda_2| - 1$. Ellipticity values approaching 0 indicate that the electron density is evenly distributed along the two directions perpendicular to the bond
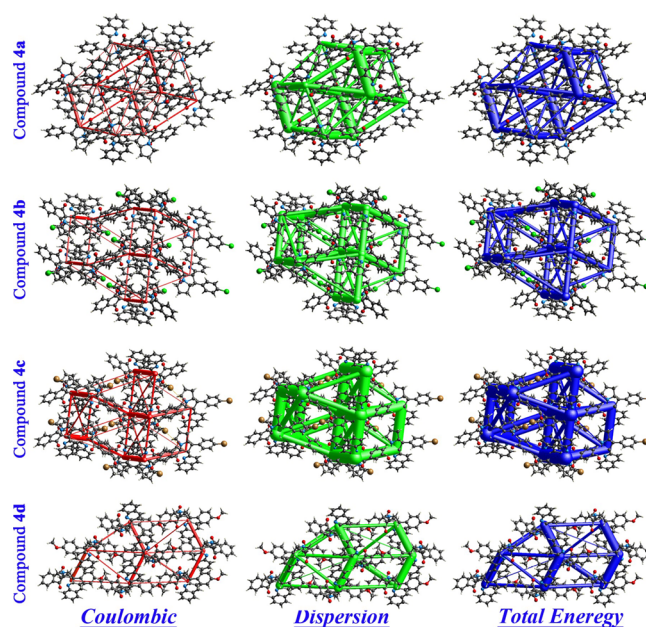
Figure 11. Energy Framework of compounds **4a−4d**. The dimensions of the tubes are set using a scale factor of 150.
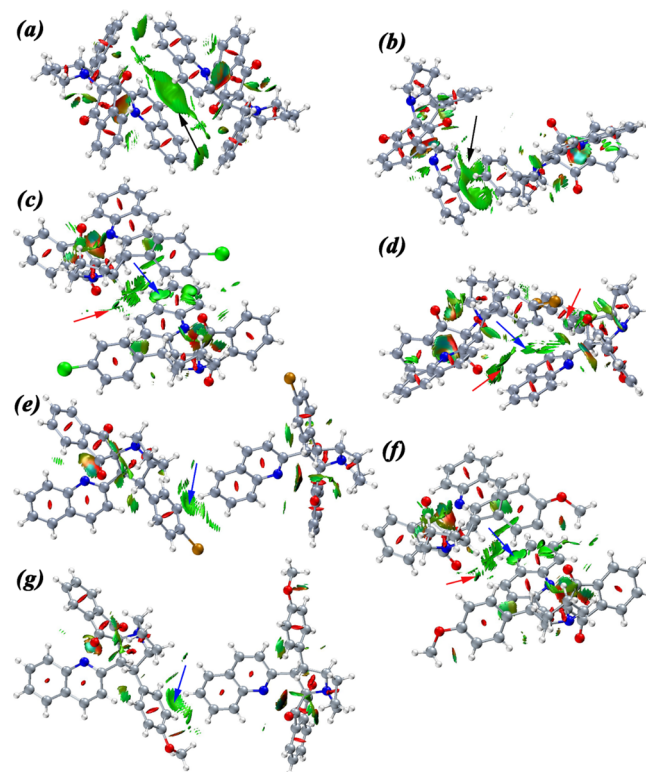
Figure 12. NCI plot index of the (a−b) compound **4a**, (c) compound **4b**, (d−e) compound **4c**, and (f−g) compound **4d**. The black, blue, and red arrows represent the $\pi\cdots\pi$, C−H⋯π, and C−H⋯O interactions.

path at the bond critical point, indicating symmetry in the interaction.[85,86] The topological parameters of the BCPs are listed in Table 6.

From Table 6, it is clearly evident that the C−H⋯O hydrogen bond interactions are more favorable than the C−H⋯π and $\pi\cdots\pi$ interactions. The C−H⋯O interaction energy varies from −1.4432 to −1.2864 kcal/mol, whereas the interaction energies
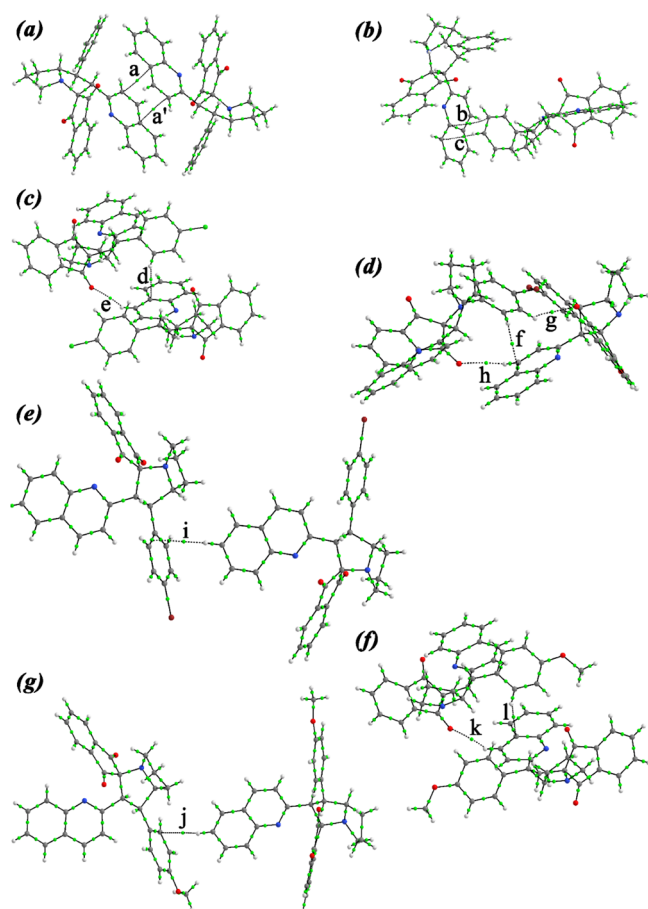
Figure 13. Distribution of bond critical points of the intermolecular interactions of (a,b) compound **4a**, (c) compound **4b**, (d,e) compound **4c**, and (f,g) compound **4d**. Green spheres represent the bond critical points.

of C−H···π and π···π interactions vary from −0.7843 to −0.6275 and −0.6589 to −0.5333 kcal/mol, respectively. In compound **4a**, the charge densities of the π···π interactions at BCPs (a, a′) have the lowest value of 0.0040 au (E_{int} = −0.5333 kcal/mol), which is a less favorable interaction than others. The most

energetic π···π interaction has an interaction energy of −0.6589 kcal/mol and a charge density of 0.0050 au at BCP (b). The bond path between the carbon atoms C2 and C28 characterizes the presence of π···π interactions, which have charge density 0.0045 au and interaction energy −0.6275 kcal/mol at the bond critical point (c). The C−H···π interactions present in both compounds **4b** and **4c** have electron densities of 0.0052 au and interaction energies of −0.7843 kcal/mol. The BCPs "j' and 'l" characterize the C−H···π interactions, which have interaction energies −0.7216 kcal/mol (ρ = 0.0047 au) and −0.6275 kcal/ mol (ρ = 0.0038 au) respectively. The BCP "e" characterizes the C7−H7···O2 interaction in compound **4b**, which has the lowest interaction energy (−1.2864 kcal/mol) among all the hydrogen bond interactions. The same C7−H7···O2 interactions in **4c** and **4d** have charge densities of 0.0076 au at BCPs "h" and "k" and interaction energies of −1.3805 kcal/mol. The most energetic C−H···O interactions, i.e., C29−H29···O1 (−1.4432 kcal/mol) characterized by BCP "g," has the highest charge density at the bond critical point (0.0076 au).

As anticipated, C−H···O interactions exhibit a greater energetic contribution compared to C−H···π interactions. This disparity arises from the inherent nature of hydrogen bonding. In C−H···O interactions, the partially positive hydrogen atom of the C−H bond can engage in a stronger electrostatic attraction with the lone pair electrons on the oxygen atom, leading to a more stable configuration and a lower energy state. Conversely, C−H···π interactions involve a weaker dispersion force with the electron cloud of an aromatic ring, resulting in a less energetically favorable interaction. This observation aligns with the well-documented strength hierarchy of noncovalent interactions, where classical hydrogen bonds typically surpass C−H···π interactions in terms of energetic contribution.[88,89]

Our research indicates that C−H···O hydrogen bond interactions exhibit lower bond ellipticity compared to π···π and C−H···π interactions. The bond ellipticity of π···π interactions ranges from 0.7415 to 2.6459, while C−H···π interactions show a broader range of 0.6857−4.8802. In stark contrast, the ellipticity values (ε) for C−H···O interactions are significantly lower, falling between 0.0406 and 0.1063. These topological parameters suggest a more even distribution of

Table 6. Topological and Energetic Properties of $\rho(r)$ Calculated at the (3, −1) Critical Point of the Intermolecular Interactions

Sl no.	interactions	ρ (a.u.)	$\nabla^2\rho$ (a.u.)	V (a.u.)	G (a.u.)	ε	H (a.u.)	$\left\|\dfrac{V}{G}\right\|$	E_{int} (kcal/mol)
compound **4a**									
1	C6···C8 (a, a′)[π···π]	0.0040	0.0108	−0.0017	0.0022	1.0033	0.0005	0.7727	−0.5333
2	C1···C27 (b)[π···π]	0.0050	0.0143	−0.0021	0.0029	0.7415	0.0008	0.7241	−0.6589
3	C2···C28 (c)[π···π]	0.0045	0.0130	−0.0020	0.0026	2.6459	0.0006	0.7692	−0.6275
compound **4b**									
4	C26−H26···C6 (d)[C−H···π]	0.0052	0.0152	−0.0025	0.0031	0.6857	0.0006	0.8064	−0.7843
5	C7−H7···O2 (e)[H−bond]	0.0072	0.0242	−0.0041	0.0051	0.0406	0.0010	0.8039	−1.2864
compound **4c**									
6	C30−H30···C6 (f)[C−H···π]	0.0052	0.0153	−0.0025	0.0032	0.7400	0.0007	0.7812	−0.7843
7	C29−H29···O1 (g)[H−bond]	0.0076	0.0275	−0.0046	0.0057	0.1063	0.0011	0.8070	−1.4432
8	C7−H7···O2 (h)[H−bond]	0.0076	0.0259	−0.0044	0.0054	0.0441	0.0010	0.8148	−1.3805
9	C4−H4···C26 (i)[C−H···π]	0.0034	0.0100	−0.0018	0.0021	4.8802	0.0003	0.8571	−0.6589
compound **4d**									
10	C30−H30···C6 (j)[C−H···π]	0.0047	0.0137	−0.0023	0.0028	0.7676	0.0005	0.8214	−0.7216
11	C7−H7···O2 (k)[H−bond]	0.0076	0.0260	−0.0044	0.0054	0.0897	0.0010	0.8148	−1.3805
12	C4−H4···C30 (l)[C−H···π]	0.0038	0.0117	−0.0020	0.0024	5.1460	0.0004	0.8333	−0.6275

electron density along the two directions perpendicular to the bond path at the bond critical point for C−H···O interactions. This observation aligns well with previous research findings, further supporting the notion of weaker bonding in C−H···O interactions compared to the other two types.[87]

The relatively low value of charge density ($\rho(r)$), a small positive value of the Laplacian ($\nabla^2\rho(r)$), and energy density ($H(r)$), and $\left|\frac{V}{G}\right| < 1$ at BCPs indicate that all non-covalent interactions are closed−shell interactions (dominated through the charge contraction away from the interatomic surface toward each nucleus).[30]

CONCLUSIONS

In conclusion, our research has yielded a comprehensive understanding of the synthesis, structural characterization, and supramolecular behavior of four quinoline-containing spiropyrrolizines synthesized via a 1,3-dipolar cycloaddition reaction. Leveraging an array of analytical techniques including ^{1}H NMR, ^{13}C NMR, HRMS, and SC-XRD, we elucidated their molecular architectures with precision. We also analyze the geometry of an additional twenty-three structures retrieved from CSD and compare them with the synthesized structures. Additionally, we delved into the realm of weak noncovalent interactions by studying supramolecular behavior. Furthermore, our exploration into weak noncovalent interactions provided deeper insights, with the PIXEL method allowing us to dissect interaction energies into Coulombic, polarization, dispersion, and repulsion components. Hirshfeld surface analysis has been performed to analyze and quantify non-covalent interactions. A comparison of the quantification of noncovalent interactions of the retrieved twenty-three compounds with the newly synthesized four compounds has also been analyzed elaborately. Within the lattice energy framework, it is discernible that the dispersion energies significantly influence the aggregate energy. Bader's theory of "Atoms in Molecules" and the NCI plot index were used to further characterize the interactions, with topological parameters at bond critical points (BCPs) providing valuable information regarding their nature and strength. These findings not only shed light on the molecular behavior of quinoline-containing spiropyrrolizines but also lay a robust foundation for future investigations into their potential applications and underlying structural dynamics. This holistic approach underscores the significance of interdisciplinary research in advancing our understanding of complex molecular systems.

ASSOCIATED CONTENT

ⓢ Supporting Information

The Supporting Information is available free of charge at https://pubs.acs.org/doi/10.1021/acsomega.4c02511.

Chiral HPLC of compound **4a** (Figure S1), NMR spectral display of compounds **4a−4d** (Figures S2−S13), bond lengths of the compounds **4a−4d** with esd (Table S1), bond angles of the compounds **4a−4d** with esd (Table S2), Overlay view of the experimental structure of compounds **4a−4d** (Figure S14), comparison of the certain bond lengths and bond angles of the compounds **4a−4d** with twenty-three compounds retrieved from CSD (Table S3), comparison of the certain torsional angle of the compounds **4a−4d** with twenty-three compounds retrieved from (Table S4), comparison of

the maximum carbon deviation from the mean plane of rings C−D, deviation of oxygen from the mean plane of rings C−D, and the angle between the mean plane of rings A and B of the compounds **4a−4d** with twenty-three compounds retrieved from CSD (Table S5), decomposed fingerprint plot of compounds **4a−4d** (Figure S15), d_{norm} surface of twenty-three compounds retrieved from CSD (Figure S16), quantification of noncovalent interactions of C···H/H···C, O···H/H···O, C···C, and N···H/H···N of compounds **4a−4d** and twenty-three compounds retrieved from CSD (Figure S17), full fingerprint plot of twenty-three compounds retrieved from CSD (Figure S18), interaction energy (kJ/mol) of the molecular pairs of compounds **4a−4d** (Table S6), energy framework calculations of compounds **4a−4d** (Figure S19), scattered graph of compounds **4a−4d** (Figure S20), and checkcif file of compound **4a−4d** (PDF)

AUTHOR INFORMATION

Corresponding Authors

Kamal K. Kapoor − *Department of Chemistry, University of Jammu, Jammu 180006, India*; Email: kamalkka@gmail.com

Saikat Kumar Seth − *Department of Physics, Jadavpur University, Kolkata 700032, India*; ⓞ orcid.org/0000-0003-4904-6926; Email: saikatk.seth@jadavpuruniversity.in

Authors

Dolma Tsering − *Department of Chemistry, University of Jammu, Jammu 180006, India*

Pratik Dey − *Department of Physics, Jadavpur University, Kolkata 700032, India*

Complete contact information is available at:
https://pubs.acs.org/10.1021/acsomega.4c02511

Author Contributions

[⊥]D.T. and P.D. contributed equally to this work. D.T. synthesized and characterized the compounds and wrote a part of the manuscript. P.D. explored the supramolecular structures, Hirshfeld surface analysis, calculated interaction energies, and lattice energies, analyzed AIM data, and NCI plots, and prepared the manuscript. K.K.K. designed the compounds, supervised the work, and reviewed the manuscript. S.K.S. coordinated the entire research work, reviewed and edited the manuscript.

Notes

The authors declare no competing financial interest.

ACKNOWLEDGMENTS

■ REFERENCES

(1) Ding, A.; Meazza, M.; Guo, H.; Yang, J. W.; Rios, R. New development in the enantioselective synthesis of spiro compounds. *Chem. Soc. Rev.* **2018**, *47*, 5946−5996.

(2) Pakravan, N.; Shayani-Jam, H.; Beiginejad, H.; Tavafi, H.; Paziresh, S. A green method for the synthesis of novel spiro compounds: Enhancement of antibacterial properties of caffeic acid through electrooxidation in the presence of barbituric acid derivatives. *J. Electroanal. Chem.* **2019**, *848*, No. 113286.

(3) Raj, A. A.; Raghunathan, R.; SrideviKumari, M. R.; Raman, N. Synthesis, Antimicrobial and Antifungal Activity of a New Class of Spiro pyrrolidines. *Bioorg. Med. Chem.* **2003**, *11*, 407−419.

(4) Safari, F.; Hosseini, H.; Bayat, M.; Ranjbar, A. Synthesis and evaluation of antimicrobial activity, cytotoxic and pro-apoptotic effects of novel spiro-4H-pyran derivatives. *RSC adv.* **2019**, *9*, 24843−24851.

(5) Alves, N. G.; Bartolo, I.; Alves, A. J.; Fontinha, D.; Francisco, D.; Lopes, S. M.; Soares, M. I.; Simões, C. J.; Prudêncio, M.; Taveira, N.; EMelo, T. M. P. Synthesis and structure-activity relationships of new chiral spiro-β-lactams highly active against HIV-1 and Plasmodium. *Eur. J. Med. Chem.* **2021**, *219*, No. 113439.

(6) Fawazy, N. G.; Panda, S. S.; Mostafa, A.; Kariuki, B. M.; Bekheit, M. S.; Moatasim, Y.; Kutkat, O.; Fayad, W.; Manawaty, M. E.; Soliman, A. A. F.; Shiekh, R. A. E.; Srour, A. M.; Barghash, R. F.; Girgis, A. S. Development of spiro-3-indolin-2-one containing compounds of antiproliferative and anti-SARS-CoV-2 properties. *Sci. Rep.* **2022**, *12*, 13880.

(7) Ye, N.; Chen, H.; Wold, E. A.; Shi, P. Y.; Zhou, J. Therapeutic Potential of Spirooxindoles as Antiviral Agents. *ACS infect. Dis.* **2016**, *2*, 382−392.

(8) Bora, D.; Kaushal, A.; Shankaraiah, N. Anticancer potential of spirocompounds in medicinal chemistry: A pentennial expedition. *Eur. J. Med. Chem.* **2021**, *215*, No. 113263.

(9) Tourneur, P.; Lucas, F.; Quinton, C.; Olivier, Y.; Lazzaroni, R.; Viville, P.; Cornil, J.; Poriel, C. Anticancer potential of spirocompounds in medicinal chemistry: A pentennial expedition. *J. Mater. Chem. C* **2020**, *8*, 14462−14468.

(10) Brouillac, C.; Shen, W. S.; Berthelot, J. R.; Jeannin, O.; Quinton, C.; Jiang, Z. Q.; Poriel, C. Spiro-configured dibenzosuberene compounds as deep-blue emitters for organic light-emitting diodes with a CIEy of 0.04. *Mater. Chem. Front.* **2022**, *6*, 1803−1813.

(11) Wang, L.; Xiong, W.; Tang, H.; Cao, D. A multistimuli-responsive fluorescent switch in the solution and solid states based on spiro[fluorene-9,9′-xanthene]-spiropyran. *J. Mater. Chem. C* **2019**, *7*, 9102−9111.

(12) Spehr, T.; Siebert, A.; Lieker, T. F.; Salbeck, J. Spiro Compounds for Organic Optoelectronics. *Chem. Rev.* **2007**, *107*, 1011−1065.

(13) Yavari, I.; Baoosi, L.; Halvagar, M. R. A synthesis of functionalized dihydro-1H-pyrrolizines and spiropyrrolizines via cyclo-addition reactions. *Mol. Divers.* **2017**, *21*, 265−271.

(14) Gutiérrez, M. R.; Domingo, L. R. Unravelling the Mysteries of the [3 + 2] Cycloaddition Reactions. *Eur. J. Org. Chem.* **2019**, *2019*, 267−282.

(15) Saraswat, P.; Jeyabalan, G.; Hassan, M. Z.; Rahman, M. U.; Nyola, N. K. Review of synthesis and various biological activities of spiro heterocyclic compounds comprising oxindole and pyrrolidine moieties. *Synth. Comun.* **2016**, *46*, 1643−1664.

(16) Ghandi, M.; Yari, A.; Jamal, S.; Rezaei, T.; Taheri, A. Synthesis of novel spiropyrrolidine/pyrrolizine-oxindole scaffolds through 1,3-dipolar cycloadditions. *Tetrahedral Lett.* **2009**, *50*, 4724−4726.

(17) Toribio, J. H.; Arraya, R. G.; Matute, B. M.; Carretero, J. C. Catalytic Asymmetric 1,3-Dipolar Cycloaddition of Azomethine Ylides with α,β-Unsaturated Ketones. *Org. Lett.* **2009**, *11*, 393−396.

(18) Breugst, M.; Reissing, H. U. The Huisgen Reaction: Milestones of the 1,3-Dipolar Cycloaddition. *Angew. Chem., Int. Ed.* **2020**, *59*, 12293−12307.

(19) Cerny, J.; Hobza, P. Non-covalent interactions in biomacromolecules. *Phys. Chem. Phys. Chem.* **2007**, *9*, 5291−5303.

(20) Hesselmann, A.; Jansen, G.; Schutz, M. Interaction Energy Contributions of H-Bonded and Stacked Structures of the AT and GC DNA Base Pairs from the Combined Density Functional Theory and Intermolecular Perturbation Theory Approach. *J. Am. Chem. Soc.* **2006**, *128*, 11730−11731.

(21) Maity, T.; Mandal, H.; Bauza, A.; Samanta, B. C.; Frontera, A.; Seth, S. K. Quantifying conventional C−H···π(aryl) and unconventional C−H···π(chelate) interactions in dinuclear Cu(ii) complexes: experimental observations, Hirshfeld surface and theoretical DFT study. *New J. Chem.* **2018**, *42*, 10202−10213.

(22) Seth, S. K.; Sarkar, D.; Kar, T. Use of π−π forces to steer the assembly of chromone derivatives into hydrogen bonded supra-molecular layers: crystal structures and Hirshfeld surface analyses. *CrystEngComm* **2011**, *13*, 4528−4535.

(23) Seth, S. K.; Sarkar, D.; Jana, A. D.; Kar, T. On the Possibility of Tuning Molecular Edges To Direct Supramolecular Self-Assembly in Coumarin Derivatives through Cooperative Weak Forces: Crystallographic and Hirshfeld Surface Analyses. *Cryst. Growth Des.* **2011**, *11*, 4837−4849.

(24) Prabhakaran, P.; Kanagasabai, S.; Seshan, G.; Gugan, K.; Usharani, S.; Rajakumar, P. Crystal Structure and Hirshfeld Surface Analysis of 1, 2, 3, Triazole Bridged Pyrrolizidine Grafted Macrocycle. *Chem. Data Collect.* **2020**, *28*, No. 100427.

(25) Pangajavalli, S.; Ranjithkumar, R.; Ramaswamy, S. Structural, Hirshfeld, Spectroscopic, Quantum Chemical, and Molecular Docking Studies on 6b′, 7′, 8′, 9′-Tetrahydro-2H, 6′H-Spiro[Acenaphthylene-1, 11′-Chromeno[3,4-a]Pyrrolizine]-2,6′(6a′H, 11a′H)-Dione. *J. Mol. Struct.* **2020**, *1209*, No. 127921.

(26) Spackman, M. A.; Jayatilaka, D. Hirshfeld surface analysis. *CrystEngComm* **2009**, *11*, 19−32.

(27) Dey, D.; Seth, S. K.; Mohan, T. P.; Chopra, D. Quantitative analysis of intermolecular interactions in crystalline substituted triazoles. *J. Mol. Struct.* **2023**, *1273*, No. 134380.

(28) Bader, R. F. Atoms in molecules. *Acc. Chem. Res.* **1985**, *18*, 9−15.

(29) Dey, P.; Islam, S.; Seth, S. K. Quantitative analysis of the interplay of hydrogen bonds in M(II)-hexaaqua complexes with HMTA [M(II) = Co(II), Mg(II); HMTA = hexamethylenetetramine]. *J. Mol. Struct.* **2023**, *1284*, No. 135448.

(30) Dey, P.; Hossain, A.; Seth, S. K. On the importance of unconventional Cu···π interaction in tetrachloro-bis(1,10-phenanthro-line)-dicopper(II) complex: Insights from experiment and theory. *J. Mol. Struct.* **2024**, *1295*, No. 136642.

(31) Sarkar, O.; Roy, M.; Pramanik, N. R.; Dey, P.; Seth, S. K.; Drew, M. G.; Chakrabarti, S. Metal-organic supramolecular architecture of oxo-bridged molybdenum(VI) complexes: synthesis, structural elucidation and Hirshfeld surface analysis. *J. Mol. Struct.* **2024**, *1301*, No. 137125.

(32) Mahajan, S.; Slathia, N.; Nuthakki, V. K.; Bharate, S. B.; Kapoor, K. K. Malononitrile-activated synthesis and anti-cholinesterase activity of styrylquinoxalin-2(1H)-ones. *RSC Adv.* **2020**, *10*, 15966−15975.

(33) CrysAlis Pro Software System, *Intelligent Data Collection and Processing Software for Small Molecule and Protein Crystallography*; Rigaku Oxford Diffraction, Rigaku Corporation: Tokyo (Japan), 2015.

(34) Bruker, *Saint Version 6.36a*; Bruker AXS Inc.: Madison, Wisconsin, USA, 2002.

(35) Bruker, *Smart Version 5.625 and SADABS, Version 2.03a*; Bruker AXS Inc.: Madison, Wisconsin, USA, 2001.

(36) Sheldrick, G. M. SHELXT − Integrated space-group and crystal-structure determination. *Acta Crystallogr. A* **2015**, *71*, 3−8.

(37) Sheldrick, G. M. Crystal structure refinement with SHELXL. *Acta Cryst. C* **2015**, *71*, 3−8.

(38) Spek, A. L. Single-crystal structure validation with the program PLATON. *J. Appl. Crystallogr.* **2003**, *36*, 7−13.

(39) Dolomanov, O. V.; Bourhis, L. J.; Gildea, R. J.; Howard, J. A.; Puschmann, H. OLEX2: a complete structure solution, refinement and analysis program. *J. Appl. Crystallogr.* **2009**, *42*, 339−341.

(40) Spackman, M. A.; McKinnon, J. J. Fingerprinting intermolecular interactions in molecular crystals. *CrystEngComm* **2002**, *4*, 378−392.

(41) McKinnon, J. J.; Jayatilaka, D.; Spackman, M. A. Towards quantitative analysis of intermolecular interactions with Hirshfeld surfaces. *Chem. Commun.* **2007**, 3814−3816.

(42) Sasan, S.; Gupta, A.; Kapoor, K. K.; Dey, P.; Seth, S. K. Synthesis, characterization, crystal structure, Hirshfeld analysis and theoretical investigation of 5-(4-methoxyphenyl)-7-phenyl-2-(pyridin-2-yl)-imidazo[1,2-a]pyridine-8-carbonitrile. *J. Mol. Struct.* **2023**, *1293*, No. 136255.

(43) Islam, S.; Dey, P.; Seth, S. K. A combined experimental and theoretical studies of two new Co(II)−PDA complexes: Unusual 2D and 3D supramolecular networks [PDA = 2,6-pyridinedicarboxylic acid]. *Polyhedron* **2023**, *242*, No. 116514.

(44) Islam, S.; Dey, P.; Das, P.; Seth, S. K. Quantitative investigations of intermolecular interactions in 2-amino-3-nitropyridine polymorphs: Inputs from quantum mechanical calculations. *J. Mol. Struct.* **2023**, *1293*, No. 136253.

(45) Dey, P.; Islam, S.; Das, P.; Seth, S. K. Structural and computational insights into two trimethylenedipyridine co-crystals: Inputs from X-ray diffraction, Hirshfeld surface, PIXEL, QTAIM and NCI plots. *J. Mol. Struct.* **2024**, *1296*, No. 136820.

(46) Islam, S.; Dey, P.; Seth, S. K. Structural Elucidation and Various Computational Studies for Quantitative Investigation of Intermolecular Interactions in Pyridine-2,6-dicarboxylic Acid and Its Di-hydrate. *J. Mol. Struct.* **2024**, *1311*, No. 138433.

(47) Frisch, M. J.; Trucks, G. W.; Schlegel, H. B.; Scuseria, G. E.; Robb, M. A.; Cheeseman, J. R.; Scalmani, G.; Barone, V.; Petersson, G. A.; Nakatsuji, H.; Li, X.; Caricato, M.; Marenich, A. V.; Bloino, J.; Janesko, B. G.; Gomperts, R.; Mennucci, B.; Hratchian, H. P.; Ortiz, J. V.; Izmaylov, A. F.; Sonnenberg, J. L.; Williams-Young, D.; Ding, F.; Lipparini, F.; Egidi, F.; Goings, J.; Peng, B.; Petrone, A.; Henderson, T.; Ranasinghe, D.; Zakrzewski, V. G.; Gao, J.; Rega, N.; Zheng, G.; Liang, W.; Hada, M.; Ehara, M.; Toyota, K.; Fukuda, R.; Hasegawa, J.; Ishida, M.; Nakajima, T.; Honda, Y.; Kitao, O.; Nakai, H.; Vreven, T.; Throssell, K.; Montgomery, Jr., J. A.; Peralta, J. E.; Ogliaro, F.; Bearpark, M. J.; Heyd, J. J.; Brothers, E. N.; Kudin, K. N.; Staroverov, V. N.; Keith, T. A.; Kobayashi, R.; Normand, J.; Raghavachari, K.; Rendell, A. P.; Burant, J. C.; Iyengar, S. S.; Tomasi, J.; Cossi, M.; Millam, J. M.; Klene, M.; Adamo, C.; Cammi, R.; Ochterski, J. W.; Martin, R. L.; Morokuma, K.; Farkas, O.; Foresman, J. B.; Fox, D. J.. *Gaussian 16, Revision C.01*; Gaussian, Inc.: Wallingford, CT, 2016.

(48) Gavezzotti, A. Efficient computer modeling of organic materials. The atom−atom, Coulomb−London−Pauli (AA-CLP) model for intermolecular electrostatic-polarization, dispersion and repulsion energies. *New J. Chem.* **2011**, *35*, 1360.

(49) Gavezzotti, A. Calculation of Intermolecular Interaction Energies by Direct Numerical Integration over Electron Densities. I. Electrostatic and Polarization Energies in Molecular Crystals. *J. Phys. Chem. B* **2002**, *106*, 4145−4154.

(50) Bader, R. F. W. A quantum theory of molecular structure and its applications. *Chem. Rev.* **1991**, *91*, 893−928.

(51) Keith, T. A. *AIMAll (Version 13.05.06)*; TK Gristmill Software: Overland Park, KS, USA, 2013.

(52) Lepetit, C.; Kahn, M. L. QTAIM and ELF topological analyses of zinc-amido complexes. *Res. Chem. Intermed.* **2021**, *47*, 377−395.

(53) Johnson, E. R.; Keinan, S.; Mori-Sanchez, P.; Contreras-Garcia, J.; Cohen, A. J.; Yang, W. Revealing Noncovalent Interactions. *J. Am. Chem. Soc.* **2010**, *132*, 6498−6506.

(54) Lu, T.; Chen, F. J. Multiwfn: A multifunctional wavefunction analyzer. *J. Comput. Chem.* **2012**, *33*, 580−592.

(55) Humphrey, W.; Dalke, A.; Schulten, K. VMD Visual molecular dynamics. *J. Mol. Graph.* **1996**, *14*, 33−38.

(56) Fábián, L.; Kálmán, A. Volumetric measure of isostructurality. *Acta Crystallogr. Sect. B Struct. Sci.* **1999**, *55*, 1099−1108.

(57) El-Emam, A. A.; Kumar, E. S.; Janani, K.; Al-Wahaibi, L. H.; Blacque, O.; El-Awady, M. I.; Al-Shaalan, N. H.; Percino, M. J.; Thamotharan, S. Quantitative Assessment of the Nature of Noncovalent Interactions in N-Substituted-5-(Adamantan-1-yl)-1,3,4-thiadiazole-2-Amines: Insights from Crystallographic and QTAIM Analysis. *RSC Adv.* **2020**, *10*, 9840−9853.

(58) Saeed, A.; Ashraf, S.; Flörke, U.; Espinoza, Z. Y. D.; Erben, M. F.; Pérez, H. Supramolecular Self-Assembly of a Coumarine-Based Acylthiourea Synthon Directed by π-Stacking Interactions: Crystal Structure and Hirshfeld Surface Analysis. *J. Mol. Struct.* **2016**, *1111*, 76−83.

(59) Latha, N.; Naga Siva Rao, J.; Raghunathan, R.; Divya, G.; Lakshmi, S. (4′-Acetyloxy-1, 3, 1′-trioxo-1, 3, 4, 4a, 4b, 5, 6, 7, 9, 9a-decahydrospiro [indene-2, 9′-pyrano [4, 3-a] pyrrolizin]-3′-yl) methyl acetate. *Acta Crystallographica Section E: Structure Reports Online* **2013**, *69* (12), o1764−o1764.

(60) Barkov, A. Y.; Zimnitskiy, N. S.; Kutyashev, I. B.; Korotaev, V. Y.; Moshkin, V. S.; Sosnovskikh, V. Y. Highly regio- and stereoselective 1,3-dipolar cycloaddition of stabilised azomethine ylides to 3,3,3-trihalogeno-1-nitropropenes: Synthesis of trihalomethylated spiroindenepyrrolidines. *J. Fluorine Chem.* **2017**, *204*, 37−44.

(61) Seshadri, P. R.; Selvanayagam, S.; Velmurugan, D.; Ravikumar, K.; Sureshbabu, A. R.; Raghunathan, R. 2′-Benzoyl-1′,2,2′,3,4′,5′,6′,6a′-octahydro-1H-indan-2-spiro-3′-(3′H-pyrrolizine)-1′-spiro-3″-1H-indoline-1,2″,3-trione. *Acta Crystallogr., Sect. E: Struct. Rep. Online* **2003**, *59* (10), o1559−o1561.

(62) Huang, F.; Zhang, F.; Xu, H. Crystal structure of spiro[(Indane-1,3-dione)-2,3′-(2′-methyl-2′-methyloxycarbonyl-hexahydro-1′H-pyrrolizine)], C18H19NO4. *Z. Kristallogr.-New Cryst. Struct.* **2012**, *227* (2), 225−226.

(63) Filatov, A. S.; Wang, S.; Khoroshilova, O. V.; Lozovskiy, S. V.; Larina, A. G.; Boitsov, V. M.; Stepakov, A. V. Stereo- and Regioselective 1,3-Dipolar Cycloaddition of the Stable Ninhydrin-Derived Azomethine Ylide to Cyclopropenes: Trapping of Unstable Cyclopropene Dipolarophiles. *J. Org. Chem.* **2019**, *84* (11), 7017−7036.

(64) Barkov, A. Y.; Zimnitskiy, N. S.; Kutyashev, I. B.; Korotaev, V. Y.; Sosnovskikh, V. Y. Regio- and Stereoselective 1,3-Dipolar Cycloaddition Reactions between Arylideneacetones and Stabilized Azomethine Ylides Obtained from Ninhydrin and Indenoquinoxalinones. *Chem. Heterocycl. Compd.* **2017**, *53*, 1315−1323.

(65) Korotaev, V. Y.; Kutyashev, I. B.; Barkov, A. Y.; Sosnovskikh, V. Y. 2-Substituted 3-Nitro-2H-Chromenes in Reaction with Azomethine Ylide Derived from Ninhydrin and Proline: Regio- and Stereoselective Synthesis of Spiro[chromeno[3,4-a]pyrrolizidine-11,2'-indene]-1',3'-diones. *Chem. Heterocycl. Compd.* **2017**, *53*, 1192−1198.

(66) Kalyanasundaram, S.; Selvanayagam, S.; Velmurugan, D.; Ravikumar, K.; Poornachandran, M.; Raghunathan, R. 2′-Benzoyl-1′-(4-Chlorophenyl)-5′,6′,7′,7a′-tetrahydrospiro[indan-2,3′(2′H)-1H-pyrrolizine]-1,3-dione. *Acta Crystallogr., Sect. E: Struct. Rep. Online* **2005**, *61* (7), o2158−o2160.

(67) Singh, C. P.; Sharma, P.; Ahmed, M.; Kumar, D.; Sharma, Y. B.; Samanta, J.; Ahmed, Z.; Shukla, S. K.; Hazra, A.; Bharitkar, Y. P. Semisynthesis of Novel Dispiro-pyrrolidino/thiopyrrolizidino-oxindolo/indanedione Natural Product Hybrids of Parthenin Followed by Their Cytotoxicity Evaluation. *ACS Omega* **2023**, *8* (38), 35283−35294.

(68) Seshadri, P. R.; Selvanayagam, S.; Velmurugan, D.; Ravikumar, K.; Sureshbabu, A. R.; Raghunathan, R. 2′-(p-Methoxybenzoyl)-2,2′,3,3′,4′,5′,6′,6a′-Octahydro-1H-Indan-2-Spiro-3′-(3′H-Pyrrolizine)-1′-Spiro-3″-1H-Indoline-1,2″,3-Trione. *Acta Crystallogr., Sect. E: Struct. Rep. Online* **2003**, *59* (11), o1783−o1785.

(69) Chandralekha, E.; Thangamani, A.; Valliappan, R. Ultrasound-Promoted Regioselective and Stereoselective Synthesis of Novel Spiroindanedionepyrrolizidines by Multicomponent 1,3-Dipolar Cycloaddition of Azomethine Ylides. *Res. Chem. Intermed.* **2013**, *39*, 961−972.

(70) Kamala, E. T. S.; Nirmala, S.; Sudha, L.; Arumugam, N.; Raghunathan, R. Ethyl 1′-[1-(4-Methoxyphenyl)-3-Phenoxy-4-Phenyl-azetidin-1-yl]-1,3-Dioxo-2′,3′,5′,6′,7′,7a′-Hexahydroindan-2-Spiro-3′-1′H-Pyrrolizine-2′-Carboxylate. *Acta Crystallogr., Sect. E: Struct. Rep. Online* **2008**, *64* (9), o1832−o1833.

(71) Ramesh, E.; Kathiresan, M.; Raghunathan, R. Solvent-Free Microwave-Assisted Conversion of Baylis−Hillman Adducts of Ninhydrin into Functionalized Spiropyrrolidines/Pyrrolizidines through 1,3-Dipolar Cycloaddition. *Tetrahedron Lett.* **2007**, *48* (10), 1835−1839.

(72) Seshadri, P. R.; Selvanayagam, S.; Velmurugan, D.; Ravikumar, K.; Sureshbabu, A. R.; Raghunathan, R. 2′-(p-Chlorobenzoyl)-

2,2′,3,3′,4′,5′,6′,6a′-Octahydro-1H-Indan-2-Spiro-3′-(1H-Pyrroli-zine)-1′-Spiro-3″-Indoline-1,2′′,3-Trione. *Acta Crystallogr., Sect. E: Struct. Rep. Online* **2004**, *60* (1), o126−o128.

(73) Giuseppetti, G.; Tadini, C.; Casaschi, A.; Faita, G. The Crystal Structure of 2-(5,7-Dichloro-1-Methyloxoindol)-3-Spiro-1′(2′-Ben-zoylhexahydropyrrolizin)-3′-Spiro-2″-Indian-1″,3″-Dione. *Z. Kristal-logr.-Cryst. Mater.* **1994**, *209* (4), 360−362.

(74) Remya, C.; Gayathri, D.; Velmurugan, D.; Ravikumar, K.; Poornachandran, M. 1′-Nitro-2′-(3-Nitrophenyl)-2′,3′,5′,6′,7′,7a′-Hexahydroindan-2-Spiro-3′-1′ H-Pyrrolizine-1,3-Dione. *Acta Crystal-logr., Sect. E: Struct. Rep. Online* **2007**, *63* (5), o2218−o2220.

(75) Satis Kumar, B. K.; Gayathri, D.; Velmurugan, D.; Ravikumar, K.; Poornachandran, M. 2′-(2-Chlorophenyl)-1′-Nitro-2′,3′,3a′,4′,5′,6′-Hexahydroindan-2-Spiro-3′-1′ H-Pyrrolizine-1,3-Dione. *Acta Crystal-logr., Sect. E: Struct. Rep. Online* **2007**, *63* (5), o2233−o2235.

(76) Zhang, L.; Quan, W.; Liu, R. M.; Tian, Y. P.; Pan, B. W.; Liu, X. L. Diastereoselective Construction of a Library of Structural Bispiro-[butyrolactone/valerolactone−pyrrolidine−indanedione] Hybrids via 1,3-Dipolar Cycloaddition Reactions. *New J. Chem.* **2022**, *46* (25), 11975−11979.

(77) Islam, S.; Das, P.; Tripathi, S.; Mukhopadhyay, S.; Seth, S. K. Exploring Solid-State Supramolecular Architectures of Penta (carbox-ymethyl) diethylenetriamine: Experimental Observation and Theoreti-cal Studies. *ChemistrySelect* **2022**, *7*, No. e202203396.

(78) Ghosh, S.; Islam, S.; Pramanik, S.; Seth, S. K. Structural elucidation of phenoxybenzaldehyde derivatives from laboratory powder X-ray diffraction: A combined experimental and theoretical quantum mechanical study. *J. Mol. Struct.* **2022**, *1268*, No. 133697.

(79) Das, P.; Islam, S.; Seth, S. K. Insights into the structural investigation of metal-complexes with 1, 3-diamino-2-hydroxypropa-netetraacetic acid: Inputs from X-ray and computational studies. *Polyhedron* **2024**, *248*, No. 116732.

(80) Das, P.; Islam, S.; Seth, S. K. Structural elucidation and interpretation of 2D−3D supramolecular assemblies featuring lone-pair··· π interaction in two Cu (II)−PDA complexes: Experimental and computational assessment. *J. Mol. Struct.* **2024**, *1308*, No. 138088.

(81) Das, P.; Rao, G. D.; Bhandary, S.; Mandal, K.; Seth, S. K.; Chopra, D. Quantitative Investigation into the Role of Intermolecular Interactions in Crystalline Fluorinated Triazoles. *Cryst. Growth Des.* **2024**, *24*, 703−721.

(82) Al-Ghulikah, H. A.; Gopalan, A.; Vahisan, L. P. S.; Khalaf, M. A.; Ghabbour, H. A.; El-Emam, A. A.; Percino, M. J.; Thamotharan, S. Insights into the Weak Csp3−H···H−Csp3Mediated Supramolecular Architecture in Ethyl 2-(5-Bromopentanamido)-4,5,6,7-Tetrahydrobenzo[b]thiophene-3-Carboxylate, a Probable Selective COX-2 Lead Molecule: An Integrated Crystallographic and Theoretical Approach. *J. Mol. Struct.* **2020**, *1199*, No. 127019.

(83) Saeed, A.; Flörke, U.; Fantoni, A.; Khurshid, A.; Pérez, H.; Erben, M. F. Close Insight into the Nature of Intermolecular Interactions in Dihydropyrimidine-2(1H)-thione Derivatives. *CrystEngComm* **2017**, *19*, 1495−1508.

(84) Benyahlou, Z. D.; Baara, F. T.; Yahiaoui, S.; Megrouss, Y.; Boukabcha, N.; Djafri, A.; Chouaih, A.; Hatzidimitriou, A. Synthesis, crystal structure, Hirshfeld surface, energy framework, NCI-RDG, theoretical calculations and molecular docking of (Z) 4, 4′-bis [-3-N-ethyl-2-N′-(phenylimino) thiazolidin-4-one] methane. *J. Mol. Struct.* **2023**, *1277*, No. 134781.

(85) Nossa González, D. L.; Gómez Castaño, J. A.; Franca, C. A.; Echeverria, G. A.; Piro, O. E.; Erben, M. F. Exploring Structural and Spectroscopic Properties of Secondary Amide Derivatives Bearing Bulky and Hydrophilic Substituents. *ChemistrySelect* **2023**, *8*, No. e202303482.

(86) Sarkar, S.; Row, T. N. G. A Heuristic Approach to Evaluate Peri Interactions versus Intermolecular Interactions in an Overcrowded Naphthalene. *IUCrJ.* **2017**, *4*, 37−49.

(87) Ajibola, A. A.; Cubillán, N.; Wojciechowska, A.; Sieroń, L.; Maniukiewicz, W. T-Shaped CH···π and antiparallel π···π interactions of Metronidazole Benzoate and Phenyl Supporting Paddle-Wheel Manganese (II) and Zinc (II) Carboxylate Complexes: Structural,

Spectroscopic, and Theoretical Studies. *J. Mol. Struct.* **2024**, *1316*, No. 138975.

(88) Gilli, G.; Gilli, P. *The Nature of the Hydrogen Bond.* Oxford University Press, 2009. .

(89) Desiraju, G. R. *Intermolecular Forces*, 2nd ed.; Oxford University Press: 2011. .